ARTICLE IN PRESS

npj Materials Degradation

https://doi.org/10.1038/s41529-026-00805-9

Article in Press

Bulk Ag addition reduces biodegradation and enhances antibacterial properties of Mg-2Zn-0.2Ca alloy

Received: 14 January 2026

Accepted: 2 May 2026

Cite this article as: Yi, F., Wu, M.-Z., Chen, Y. *et al.* Bulk Ag addition reduces biodegradation and enhances antibacterial properties of Mg-2Zn-0.2Ca alloy. *npj Mater Degrad* (2026). https://doi.org/10.1038/s41529-026-00805-9

Fang Yi, Meng-Zhi Wu, Yi Chen, Lingzhi Yang, Jing Guo & Yonghao Gao

We are providing an unedited version of this manuscript to give early access to its findings. Before final publication, the manuscript will undergo further editing. Please note there may be errors present which affect the content, and all legal disclaimers apply.

If this paper is publishing under a Transparent Peer Review model then Peer Review reports will publish with the final article.

ARTICLE IN PRESS

© The Author(s) 2026. **Open Access** This article is licensed under a Creative Commons Attribution-NonCommercial-NoDerivatives 4.0 International License, which permits any non-commercial use, sharing, distribution and reproduction in any medium or format, as long as you give appropriate credit to the original author(s) and the source, provide a link to the Creative Commons licence, and indicate if you modified the licensed material. You do not have permission under this licence to share adapted material derived from this article or parts of it. The images or other third party material in this article are included in the article's Creative Commons licence, unless indicated otherwise in a credit line to the material. If material is not included in the article's Creative Commons licence and your intended use is not permitted by statutory regulation or exceeds the permitted use, you will need to obtain permission directly from the copyright holder. To view a copy of this licence, visit http://creativecommons.org/licenses/by-nc-nd/4.0/.

ARTICLE IN PRESS

Bulk Ag Addition Reduces Biodegradation and Enhances Antibacterial Properties of Mg-2Zn-0.2Ca Alloy

Fang Yi[1,5,6], Meng-Zhi Wu[3], Yi Chen[2], Lingzhi Yang[4], Jing Guo[1], Yonghao Gao[2,*]

[1] Xiangya School of Stomatology, Central South University, Changsha 410008, Hunan, China

[2] School of Materials Science and Engineering, Central South University, Changsha 410083, China

[3] National Medical Metabolomics International Collaborative Research Center, Xiangya Hospital, Central South University, Changsha, Hunan, China

[4] School of Minerals Processing and Bioengineering, Central South University, Hunan, Changsha 410083, China

[5] Hunan Clinical Research Center of Oral Major Diseases and Oral Health, Changsha 410008, China

[6] Hunan Xiangya Stomatological Hospital, Central South University, Changsha 410008, China

* Correspondence: gaoyonghao_009@163.com

Abstract: Mg-Zn-Ca alloys are attractive biodegradable metals but suffer from accelerated degradation and limited antibacterial functionality under physiological environments. Here, minor Ag additions (0, 0.1, 0.3 and 0.5 wt.%) were introduced into an as-cast Mg-2Zn-0.2Ca alloy to regulate degradation behavior and antibacterial performance. Electrochemical and immersion results show that 0.1 wt.% Ag stabilizes the corrosion product layer, suppresses localized degradation, and reduces the corrosion rate to 0.12 ± 0.02 mm/year. Increasing Ag content progressively enhances antibacterial activity against *Escherichia coli* and *Staphylococcus aureus*, with antibacterial efficiencies rising from 61.4 ± 3.9% (Ag-free) to 89.6 ± 3.0% at 0.1 wt.% Ag and exceeding 99% at 0.3-0.5 wt.% Ag. The improved antibacterial performance correlates with increased Ag^+ release during degradation, while excessive Ag promotes micro-galvanic effects that accelerate corrosion. These results elucidate the competing roles of Ag in governing degradation kinetics and antibacterial efficacy, providing useful insight for designing multifunctional biodegradable Mg alloys.

Keywords: Mg-Zn-Ca alloy; biodegradable metal; corrosion rate; antibacterial property

Introduction

Traditional metallic implants made from stainless steels, titanium (Ti) and their alloys are widely used in clinical fixation of bone defects owing to their high mechanical strength and durability. However, these permanent implants are largely biologically inert, unable to actively promote tissue regeneration, and often lead to stress-shielding due to their elastic moduli being significantly higher than that of natural bone, which can cause peri-implant bone resorption and delayed healing[1,2]. For temporary orthopedic fixation devices such as plates and screws, the lack of degradability often necessitates a secondary surgical procedure for implant removal after fracture healing, thereby increasing medical risks and healthcare costs[3,4]. Moreover, conventional metallic implants are prone to bacterial adhesion and subsequent biofilm formation, which may lead to persistent implant-associated infections requiring prolonged antibiotic treatment and may further contribute to antibiotic resistance. Clinical reports indicate that implant-associated infections remain a major complication in orthopedic surgery, although the incidence varies

ARTICLE IN PRESS

markedly with the clinical scenario and can be particularly high in severe open fractures, where reported infection rates may exceed 15%[5] and, in some reports, reach much higher levels[6]. These clinical challenges underscore the need for effective antibacterial strategies. Accordingly, increasing attention has been directed toward biodegradable metallic implants that can provide temporary mechanical support while also offering antibacterial functionality.

Magnesium (Mg) and its alloys have emerged as promising candidates for biodegradable orthopedic implants due to their advantageous combination of biocompatibility, bioactivity, and an elastic modulus close to that of cortical bone, which helps mitigate stress-shielding effects[7-10]. Mg alloys undergo controlled corrosion in physiological environments[11], resulting in gradual loss of mechanical integrity synchronized with tissue healing and enabling eventual resorption without the need for implant removal[12]. However, the rapid and heterogeneous degradation of many Mg alloys in chloride-rich body fluids remains the principal challenge limiting their clinical translation, as accelerated corrosion can lead to excessive hydrogen gas evolution, localized alkalization and premature mechanical failure before complete bone regeneration. Consequently, controlling the degradation rate of Mg alloys while maintaining desirable mechanical and biological properties continues to be a key focus in biomaterials research.

Alloying has been widely recognized as an effective strategy to tailor the degradation and mechanical characteristics of Mg alloys[13]. Among the alloying elements investigated, zinc (Zn) and calcium (Ca) are particularly attractive because they are essential trace elements in human physiology and play indispensable roles in bone metabolism. Zn also possesses intrinsic antibacterial activity. The release of Zn^{2+} ions can disrupt bacterial membrane integrity and interfere with essential metabolic processes[14]. Zn addition into Mg can enhance mechanical performance through solid-solution and precipitation strengthening and has been associated with reduced corrosion rates when optimized below certain concentrations[15-17]. Ca can react with Mg and Zn to form stable intermetallic phases that refine the microstructure and improve strength, and low Ca levels (e.g., <1 wt%) show good biocompatibility without compromising corrosion resistance[18,19]. In particular, Mg-2Zn-0.2Ca was selected as the baseline composition because it provides a suitable balance between mechanical performance and microstructural stability. At this composition, the low Ca content (~0.2 wt.%) helps suppress excessive formation of brittle Mg_2Ca along grain boundaries while allowing sufficient $Ca_2Mg_6Zn_3$ precipitation to strengthen the alloy. Meanwhile, Zn at 2 wt.% provides solid-solution strengthening and is beneficial for improving ductility and fracture tolerance[20-22]. Prior research on Mg-Zn-Ca systems has identified compositions such as Mg-2Zn-0.2Ca that exhibit a favorable balance between mechanical strength, degradation behavior and cytocompatibility, making them attractive for biodegradable implant applications[20,23]. Additional studies have demonstrated that appropriately designed Mg-Zn-Ca formulations can promote bone cell adhesion and proliferation, while simultaneously mitigating adverse corrosion behavior[24]. Nevertheless, improvement of functional properties, especially antibacterial activity, is still needed for broader clinical application.

Incorporating antibacterial functionality into biodegradable Mg alloys is critical to addressing peri-implant infections without reliance on systemic antibiotics. Metal ions provide broad-spectrum antibacterial activity by disrupting microbial cell membranes and biochemical pathways,

ARTICLE IN PRESS

and unlike antibiotics they are less prone to resistance development[25]. Silver (Ag), a biologically tolerated trace element, has been shown to endow alloys with effective antibacterial properties while contributing to microstructural refinement, grain size reduction and mechanical strengthening through the promotion of fine precipitates[26]. Prior studies have shown that minor additions of Ag to Mg-Zn-Ca alloys can enhance antibacterial performance while maintaining acceptable biocompatibility[26-29]. However, the detailed dose-dependent relationship between Ag release, antibacterial efficacy, and cytocompatibility remains insufficiently understood, and the reported effects of Ag on corrosion resistance are not fully consistent across the literature[27,30-32]. Small Ag additions (<0.5 wt.%) are generally unlikely to form independent new phases, but can modify the nucleation and distribution of existing precipitates, thereby accelerating precipitation kinetics and refining the microstructure, which may improve strength and hardness[26,33,34]. In contrast, very low Ag additions (<0.1 wt.%) may be insufficient to provide a clear antibacterial effect, whereas excessive additions (>0.5 wt.%) may increase Ag enrichment in second phases and thus aggravate micro-galvanic corrosion, resulting in reduced corrosion resistance[27,35,36]. This is consistent with previous studies showing that Ag can either improve or deteriorate corrosion behavior depending on the alloy composition and microstructural condition[26,37]. Such discrepancies underscore the need for systematically evaluating the effect of Ag on balancing antibacterial function and biodegradation in Mg-Zn-Ca systems.

In the present study, as-cast Mg-2Zn-0.2Ca-xAg (x = 0, 0.1, 0.3, 0.5 wt.%) alloys were developed as biodegradable metals to clarify the effects of minor Ag additions on microstructure, corrosion behavior, and antibacterial properties. Microstructural characterization, electrochemical testing, immersion and mass-loss measurements in Hank's solution, and antibacterial assays were performed to elucidate the mechanisms underlying alloy degradation and bactericidal performance. Unlike our previous studies on extruded alloys[23,38], which focused on processing-induced microstructural evolution, mechanical properties, and corrosion behavior after thermomechanical treatment, the present work examines the intrinsic degradation behavior and antibacterial performance of the as-cast alloys. Together, these studies provide complementary insight into the structure-degradation-function relationship of this alloy system and may guide the design of biodegradable Mg alloys with balanced corrosion control and antibacterial activity for orthopedic fixation.

Results

Microstructure characterization

Fig. 1 demonstrates the optical microstructure of the as-cast Mg-2Zn-0.2Ca-*x*Ag alloys. A large number of discontinuously distributed secondary phases were observed along the grain boundaries, accompanied by a small amount of spherical secondary phases within the grains. The second dendrite arm spacing of the alloys was measured using the linear intercept method in accordance with ASTM E112-10. The average second dendrite arm spacing of the as-cast ZX20, ZXQ0.1, ZXQ0.3 and ZXQ0.5 alloys were 71.0 ± 24.9 μm, 86.0 ± 24.2 μm, 78.1 ± 21.7 μm, and 86.8 ± 23.3 μm, respectively (Fig. 2a), indicating that the trace addition of Ag slightly increased the second dendrite arm spacing of the as-cast alloys. The effect of Ag addition on the as-cast

ARTICLE IN PRESS

microstructure is mainly reflected in the evolution of dendritic morphology, particularly the variation in secondary dendrite arm spacing (SDAS), rather than in obvious changes in eutectic morphology. Because Ag has limited solubility in the α-Mg matrix, it is expected to partition into the $Ca_2Mg_6Zn_3$ phase during solidification, thereby modifying local solute redistribution and affecting dendritic growth behavior. As a result, the SDAS shows a non-monotonic variation with increasing Ag content, suggesting a competitive effect between solute segregation and growth restriction. The volume fractions of the secondary phases in ZX20, ZXQ0.1, ZXQ0.3, and ZXQ0.5 were 3.5 ± 0.3%, 3.7 ± 0.4%, 4.0 ± 0.3%, and 2.3 ± 0.02%, respectively (Fig. 2b). However, the morphology and spatial distribution of the eutectic phases remain essentially unchanged with Ag addition (≤0.5 wt.%). This indicates that Ag does not alter the fundamental solidification path, but mainly influences dendritic growth kinetics through its redistribution within the pre-existing secondary phases.

Fig. 3 shows the SEM micrographs and compositional analyses of selected micro-regions of the as-cast Mg-2Zn-0.2Ca-*x*Ag (*x* = 0, 0.1, 0.3, 0.5 wt.%) alloys. A bright secondary phase, discontinuously distributed along the grain boundaries, is clearly visible, while only a limited amount of secondary phase is observed within the grains. Elemental analysis revealed pronounced segregation of Zn and Ca within the secondary phase (Table 1). Based on the Mg-Zn-Ca ternary phase diagram, this secondary phase is inferred to be $Ca_2Mg_6Zn_3$. Moreover, EDS results also indicated co-segregation of Ag with Zn and Ca, and the Ag concentration within the secondary phase increased progressively with increasing nominal Ag content in the alloy. Specifically, the Ag contents in the secondary phases of ZXQ0.1, ZXQ0.3, and ZXQ0.5 alloys were 0.4 at.%, 0.8 at.%, and 2.5 at.% , respectively (corresponding to points 4, 7 and 11 in Fig. 3; Table 1). The volume fractions of the secondary phases quantified from SEM images using ImageJ software are shown in Fig. 2b. The values were 3.5 ± 0.3%, 3.7 ± 0.4%, 4.0 ± 0.3%, and 2.3 ± 0.02% for ZX20, ZXQ0.1, ZXQ0.3, and ZXQ0.5 alloys, respectively. Trace additions of Ag (0.1 wt.% and 0.3 wt.%) resulted in an increase in the secondary phase fraction, whereas further increasing Ag content significantly reduced the secondary phase volume fraction to below that of the Ag-free alloy, with ZXQ0.3 exhibiting the highest secondary phase content. This non-monotonic variation suggests that Ag influences the solidification behavior and solute redistribution of the Mg-Zn-Ca system, thereby affecting competitive phase formation and stability.

To further investigate the effect of Ag addition on phase constitution, XRD analysis was performed, and the results are presented in Fig. 4. All alloys exhibited similar phase compositions. The as-cast ZX20, ZXQ0.1, ZXQ0.3, and ZXQ0.5 alloys were predominantly composed of an α-Mg matrix, and no new Ag-containing phases were detected. Diffraction peaks located at 2θ = 32.5°, 34.8°, 37.0°, and 48.2° correspond to the $(10\bar{1}0)$, (0002), $(10\bar{1}1)$, and $(10\bar{1}2)$ planes of α-Mg, respectively. In addition, characteristic diffraction peaks appeared at 2θ = 21.4° and 41.5°, corresponding to the (200) and (222) planes of $Ca_2Mg_6Zn_3$, confirming the presence of this phase in the as-cast alloys; however, these peaks were relatively weak due to their limited contents compared with the dominant α-Mg matrix. The weak yet distinct reflections further validate the consistency between XRD and EDS observations, supporting the presence of $Ca_2Mg_6Zn_3$ as a stable grain boundary phase in the studied composition range.

ARTICLE IN PRESS

Electrochemical characterization

Fig. 5(a) shows the variation in OCP of the as-cast Mg-2Zn-0.2Ca-*x*Ag (*x* = 0, 0.1, 0.3, 0.5 wt.%) alloys during immersion in Hank's solution at 37.0 ± 0.5 °C for 12 h. A sharp increase in OCP was observed in the initial immersion stage, indicating the rapid passivation of the alloys, which shifts the mixed potential toward a more positive direction. After approximately 900 s, the OCP reached a peak value, followed by a gradual decrease attributed to localized film breakdown and the initiation of pitting corrosion. Subsequently, the alternating formation of new corrosion products and the detachment of unstable products resulted in OCP fluctuations. The stabilized OCP values of the alloys showed limited differences: ZX20 and ZXQ0.1 exhibited similar OCP values of approximately -1.60 V, while ZXQ0.5 displayed a slightly higher value of -1.59 V and reached its peak more rapidly, suggesting a faster initial electrochemical response and more rapid surface film evolution. This behavior suggests that although Ag promotes initial film formation, excessive Ag content may simultaneously accelerate localized film instability.

Fig. 5(b) presents the PDP curves of the alloys after 12 h immersion. Compared with ZX20, ZXQ0.5 exhibited a more positive E_{corr} consistent with the OCP results. All alloys displayed weak passivation behavior in the anodic region, indicative of the formation of a protective corrosion product film. A passive-active transition was observed in each anodic branch, corresponding to film breakdown. The stability of the film was evaluated using the potential difference between E_{corr} and E_{break}. ZXQ0.1 exhibited the largest potential difference (0.139 V), followed by ZX20 and ZXQ0.3, whereas ZXQ0.5 showed the smallest difference (0.03 V), suggesting inferior stability of its product film. Therefore, the addition of 0.1 wt.% Ag improves film stability, whereas higher Ag contents promote film instability and facilitate rupture.

Because no reliable linear anodic Tafel region was observed, only the relatively stable quasi-linear cathodic segments near E_{corr} were used for approximate extrapolation to estimate i_{corr} (Table 2). The same fitting criterion was applied to all alloys, enabling consistent comparative analysis, although these cathodic segments did not represent fully developed classical Tafel regions. The fitted cathodic Tafel slopes (βc) were -224.41 ± 5.16, -221.58 ± 19.95, -297.55 ± 18.32 and -205.25 ± 38.59 $mV \cdot dec^{-1}$ for ZX20, ZXQ0.1, ZXQ0.3 and ZXQ0.5, respectively. Combined with the estimated i_{corr} values, these results suggesting a lower short-term electrochemical corrosion tendency, whereas ZXQ0.5 exhibited an approximately an order of magnitude higher i_{corr} than ZXQ0.1, indicating substantially accelerated degradation. Both i_{corr} and weight-loss results consistently show that 0.1 wt.% Ag slightly reduces the degradation rate, whereas 0.3 wt.% and 0.5 wt.% Ag significantly accelerate degradation.

Fig. 5(c, d) shows the EIS spectra after 12 h immersion. The Nyquist semicircle diameter varied significantly with Ag content. The semicircle of ZXQ0.1 expanded markedly, whereas those of ZXQ0.3 and ZXQ0.5 progressively decreased, indicating reduced corrosion resistance. Generally, a larger Nyquist diameter corresponds to superior corrosion resistance; thus, ZXQ0.1 exhibits the lowest degradation rate, while ZXQ0.5 shows the highest, consistent with PDP results. The Bode impedance modulus plots further confirm this corrosion trend. ZXQ0.1 exhibits the highest impedance modulus in the low-frequency region, whereas ZXQ0.3 and ZXQ0.5 show markedly reduced values. Since the low-frequency impedance modulus reflects the overall

ARTICLE IN PRESS

corrosion resistance of the alloy/electrolyte interface, including the barrier performance of the corrosion product layer, these results indicate that minor Ag addition improves film protectiveness, while excessive Ag weakens the barrier effect. The Bode phase-angle spectra provide further insight into the interfacial corrosion process. ZXQ0.1 shows the phase-angle maximum at the lowest frequency, suggesting a slower interfacial electrochemical response and a longer characteristic relaxation time. This suggests that the surface film formed on ZXQ0.1 is more stable and more effective in retarding electrochemical reactions. In contrast, the phase-angle maxima of ZXQ0.3 and ZXQ0.5 shift toward higher frequencies, suggesting faster interfacial electrochemical kinetics and reduced surface-film protectiveness. This interpretation is consistent with their lower low-frequency impedance modulus values.

The EIS spectra were fitted using the equivalent circuit shown in Fig. 5(c). Here, R_s represents the solution resistance; R_{ct} and CPE_{dl} correspond to charge transfer resistance and double-layer capacitance; R_f and CPE_f represent the resistance and capacitance of the surface product film; and the R_L-L series simulates adsorption/desorption-related impedance. The experimental EIS spectra were fitted against the proposed equivalent circuit, and the fitting parameters are listed in Table 3. Robust fitting goodness has been verified by the χ^2 shown in Table 3. The total resistance R_p (R_f + R_{ct}) is widely used to assess corrosion resistance, and $1/R_p$ can be correlated with corrosion rate[39] . In general, higher R_p values indicate better protective ability of corrosion products on Mg alloys[40]. The result shows that R_p increased with 0.1 wt.% Ag, whereas a further increase in Ag content led to a reduction in R_p. Overall, these findings indicate a degradation trend characterized by "initial improvement followed by deterioration", confirming that ZXQ0.1 exhibits the most favorable corrosion resistance among the as-cast alloys.

The R_{ct} values obtained from equivalent-circuit fitting increase at 0.1 wt.% Ag but decrease significantly at higher Ag contents, confirming that minor Ag addition suppresses interfacial charge-transfer kinetics, whereas excessive Ag accelerates electrochemical reactions. Combined with the increased $\boldsymbol{i_{corr}}$ values for ZXQ0.3 and ZXQ0.5, these results suggest intensified micro-galvanic coupling between Ag-enriched second phases and the Mg matrix at higher Ag levels. Overall, the trends in low-frequency |Z|, characteristic phase-angle frequency, R_{ct}, R_p, and i_{corr} consistently support an initial improvement followed by deterioration in corrosion resistance, confirming that ZXQ0.1 exhibits the most favorable corrosion resistance among the investigated alloys.

In vitro corrosion behavior analysis

The detailed corrosion rates and corresponding mass-loss data of the as-cast alloys are summarized in Table 4. Fig. 6(a, b) presents the average corrosion rates and the mass loss of the alloys, determined from weight-loss measurements after immersion in Hank's solution for 168 h. Compared with the Ag-free ZX20 alloy, the alloy containing 0.1 wt.% Ag (ZXQ0.1) exhibited a comparable corrosion rate at 168 h, with only a slight tendency toward reduction. A modest decrease in long-term corrosion rate was further observed at 672 h (Table 4). In contrast, when the Ag content increased to 0.3 wt.% and 0.5 wt.%, the corrosion rate markedly increased. Although the absolute corrosion rates derived from electrochemical and weight-loss measurements differed, both methods showed a consistent ranking of alloy degradation behavior, which reflects the

ARTICLE IN PRESS

distinction between instantaneous electrochemical response and cumulative mass loss during immersion.

Magnesium alloy degradation inherently generates hydroxyl ions (OH^-), elevating the surrounding pH. Such pH changes not only reflect corrosion progress but also significantly influence cellular responses and osteogenesis. In this study, the pH evolution of Hank's solution during immersion was monitored to assess degradation behavior of the Mg-2Zn-0.2Ca-*x*Ag alloys. As shown in Fig. 6(c), the pH variation over 168 h at 37 °C displays three distinct phases: an initial rapid rise due to aggressive Mg dissolution (0-12 h), a moderated increase as corrosion products form, and a slight late-stage decline potentially due to OH^- consumption during secondary product transformations (as will be confirmed by XRD evaluation of the corroded samples). Notably, ZXQ0.1 maintained lower pH than other samples during the first 168 h, with final pH values of 9.36 ± 0.52 (ZX20), 9.25 ± 0.45 (ZXQ0.1), 9.41 ± 0.42 (ZXQ0.3), and 9.61 ± 0.40 (ZXQ0.5), indicating slowed degradation in the 0.1 wt.% Ag alloy.

Magnesium alloys continuously release Mg^{2+} ions during degradation; thus, monitoring Mg^{2+} concentration evolution provides another important indicator of degradation behavior, while also being biologically relevant owing to its regulatory effects on cellular activity. As shown in Fig. 6(d), the initial Mg^{2+} concentration in Hank's solution was 23.0 ± 0.3 mg/L. As immersion progressed, Mg^{2+} concentration gradually increased with ongoing corrosion. A rapid increase occurred within the first 12 h, indicating vigorous early dissolution. Thereafter, the growth rate slowed, implying that the formation of corrosion products partially consumed Mg^{2+} and provided a temporary protective barrier, thereby establishing a dynamic balance between dissolution and consumption. After 120 h, Mg^{2+} concentration increased more rapidly again, suggesting renewed degradation, possibly due to detachment of accumulated corrosion products from the alloy surface. As shown in Fig. 6(d), the Mg^{2+} concentration for ZXQ0.1 remained the lowest throughout immersion; after 168 h, Mg^{2+} concentrations for ZX20, ZXQ0.1, ZXQ0.3, and ZXQ0.5 were 49.7 ± 2.6, 42.8 ± 1.8, 51.1 ± 0.1, and 58.8 ± 2.3 mg/L, respectively, which is consistent with the weight-loss data.

Fig. 7 presents the macroscopic morphologies of the alloys after immersion, with dark regions corresponding to corroded areas that progressively expanded over time, indicating a nonuniform degradation pattern. In ZX20, only a few discrete corrosion pits were observed after 12 h, suggesting predominant pitting corrosion. With extended immersion, both the number and size of pits increased, though large areas of uncorroded matrix still remained after 168 h, indicating relatively slow lateral propagation. Surface corroded areas were statistically analyzed using three independent samples for each alloy (Fig. 8), reflecting the lateral spread of corrosion over the sample surface. Within the first 72 h, corrosion coverage remained below ~4%, indicating slow lateral expansion. Beyond 72 h, the slope of the corrosion-time curve increased, indicating accelerated propagation, especially between 120-168 h, when corrosion area increased by ~12-15% per 48 h. ZX20 tended to show a larger corroded surface fraction, although no statistically significant differences were observed among the alloys. This is likely because surface coverage reflects lateral corrosion spreading rather than corrosion depth or total material loss. ZX20 mainly exhibited relatively uniform and shallow corrosion, leading to broader surface coverage.

ARTICLE IN PRESS

In contrast, ZXQ0.3 and ZXQ0.5 showed smaller corroded surface fractions, indicating that corrosion was more localized than uniformly distributed. Therefore, surface observations alone reveal only part of the degradation behavior, and further evaluation of corrosion depth and material loss is necessary for a comprehensive assessment.

To further determine whether the reduced surface corrosion fraction in ZXQ0.3 and ZXQ0.5 reflects milder degradation or a change in corrosion mode, three-dimensional tomographic analysis was conducted to evaluate corrosion penetration depth. Fig. 9(a-d) shows three-dimensional topography of the as-cast alloys after 14 days of immersion in Hank's solution at 37.0 ± 0.5 °C, following removal of corrosion products. Discrete pitting corrosion was observed on the alloy surfaces, with significant variation in pit depth. The depth distribution of the deepest pits for each alloy is shown in Fig. 9(e). The maximum corrosion depths of ZX20, ZXQ0.1, ZXQ0.3, and ZXQ0.5 were 170 μm, 239 μm, 265 μm, and 322 μm, respectively, indicating that Ag addition increased localized corrosion depth.

Fig. 10 shows the SEM images of the as-cast alloys after immersion in Hank's solution for 168 h. In each column, the image on the right represents a magnified view of the region indicated by the yellow arrow in the left image. During degradation, the primary corrosion mode of the as-cast alloys was pitting, initiated near the secondary phases due to micro-galvanic effects. Initially, the α-Mg matrix acted as the anode, gradually losing electrons and dissolving, while the secondary phases, having higher electrochemical potential, served as cathodic sites**.** This galvanic interaction, accompanied by electron transfer, caused the α-Mg regions in contact with the secondary phases to be preferentially corroded. Subsequently, the α-Mg adjacent to grain boundaries acted as anodic regions, further losing electrons and undergoing corrosion. As shown in Fig. 10, this process continued until the surrounding α-Mg matrix was consumed, ultimately forming pits comparable in size to the grains, after removal of corrosion products. All alloys exhibited accumulated corrosion products containing spherical and irregular phases, underlain by relatively dense product films.

Table 5 shows the EDS results of the corrosion products, confirming the presence of Mg, O, Ca, P, and C, reminder of $Mg(OH)_2$ and hydroxyapatite (HA) species[39,41,42], which was later validated by XRD. The addition of Ag did not change the overall composition of the corrosion products but enhanced Ca and P deposition on the alloy surface, indicating more pronounced accumulation of phosphate and carbonate species. Through continuous deposition of calcium and phosphate ions and their gradual mineralization into HA, the alloy creates a bone-like microenvironment that supports osteoblast attachment, thereby potentially promoting the repair of defect sites[43]. These results suggest that Ag incorporation may enhance the osteogenic potential of the alloy surface. After removal of the surface films, numerous pits and micro-pores remained, serving as pathways for electrolyte penetration and accelerating pit propagation, particularly in ZXQ0.3 and ZXQ0.5.

The cross-sectional morphologies and elemental distributions of the as-cast alloys after immersion in Hank's solution for 168 h are shown in Fig. 11(a-d). Low-magnification overviews reveal that the ZXQ0.1 alloy exhibits the smallest proportion of locally corroded regions (27%) after the addition of 0.1 wt.% Ag, whereas the fraction of localized corrosion areas increases

ARTICLE IN PRESS

dramatically to 75% when the Ag content reaches 0.5 wt.%. Distinct corrosion pits with discrete spatial distribution were observed across all samples. For the ZX20 alloy, the maximum pit depth reached 184 μm. After introducing 0.1 wt.% Ag, ZXQ0.1 showed a corrosion morphology similar to ZX20, but with slightly reduced pit depth (170 μm). When the Ag content increased to 0.3 wt.%, the ZXQ0.3 alloy exhibited a markedly altered degradation profile, characterized by a significant increase in the number of corrosion pits and reduced spacing between adjacent pits, with the deepest pit extending up to 281 μm. Further increasing the Ag content to 0.5 wt.% led to a higher pit density within the selected cross-sectional area, whereas the average size of individual pits decreased, together with a reduction in the maximum pit depth compared with the 0.3 wt.% alloy.

To clarify the composition of the degradation products, the alloys were immersed in Hank's solution for 672 h, after which the surface corrosion products were analyzed by XRD and XPS. The XRD spectra are shown in Fig. 12, indicating that the alloy surfaces mainly consisted of Mg, along with $Mg(OH)_2$ and hydroxyapatite ($Ca_{10}(PO_4)_6(OH)_2$, HA). Wang et al. [44] reported that the thickness of MgO is typically very low and that it is usually covered by $Mg(OH)_2$, which explains why MgO was not detected by XRD. With the addition of 0.1 wt.% Ag, the α-Mg matrix in ZXQ0.1 exhibited the strongest XRD signal, while further increases in Ag content resulted in thicker corrosion product layers, leading to weaker α-Mg signals and a relative increase in the diffraction peak intensities of $Mg(OH)_2$, HA, and other corrosion products.

The chemical composition of the samples after immersion in Hank's solution for 28 days was analyzed by XPS. Mg, O, Ca, P, and C were identified in the XPS survey spectra. The corresponding high-resolution spectra of each element are presented in Fig. 13. The spectra shown in the left column were obtained from the ZX20 alloy, whereas those in the right column correspond to the ZXQ0.5 alloy. The binding energy of the C 1s transition associated with adventitious carbon was calibrated to 284.8 eV. The C 1*s* spectra of the two samples exhibited similar characteristics, featuring doublet peaks that were deconvoluted into three sub-peaks with binding energies of 284.8 eV, 286.2 eV, and 289.0 eV (with a BE deviation of ±0.2 eV), suggesting the presence of C-C, C-O-C, and CO_3^{2-} compounds, respectively. The O 1s spectra acquired from both samples exhibited a single, well-defined peak with excellent Gaussian symmetry. The deconvolution analysis of the O1s peak revealed two sub-peaks at binding energies around 531.5 ± 0.2 eV and 532.4 ± 0.1 eV, which can be attributed to PO_4^{3-} and OH^- [45], respectively. The P 2*p* signal obtained from the ZX20 alloy exhibited greater spectral noise and a poorer signal-to-noise ratio compared to that of the ZXQ0.5 alloy. Nevertheless, the characteristic peak profile remained discernible around BE = 133.4 eV, confirming the presence of PO_4^{3-} compounds [46] - a finding consistent with the O 1s spectral analysis. The P 2*p* profile was resolved into two peaks associated with the spin-orbit components of P $2p_{1/2}$ (BE=134.1 ± 0.1 eV) and P $2p_{3/2}$ (133.1 ± 0.1 eV). The Ca 2*p* profile are also presented in Fig.13. The Ca 2*p* profile of the ZX20 alloy present a broad peak with a distinct shoulder at the lower-binding-energy side, while that of the ZXQ0.5 alloy exhibits two well-resolved peaks. Given the presence of Mg on the sample surface, the acquired Ca 2*p* signal is inevitably affected by the overlapping Mg KLL Auger region. Consequently, the Ca 2*p* spectrum was deconvoluted into three components, corresponding to the Mg KLL transition (351.7 ± 0.1 eV), Ca $2p_{3/2}$ (347.4 eV), and Ca $2p_{1/2}$ (350.9 eV). The deconvolution was rigorously

ARTICLE IN PRESS

constrained by fixing the spin-orbit splitting (Ca $2p_{1/2}$ - Ca $2p_{3/2}$) at 3.55 eV and the peak-area ratio at 0.5. The Ca $2p_{3/2}$ at BE = 347.4 eV suggests the presence of Ca in the form of hydroxyapatite (HA) on the sample surface [45], which further corroborated the identification of OH^- and PO_4^{3-} compounds derived from the O 1*s* and P 2*p* spectral analysis. The Mg KLL Auger spectrum at BE = 351.7 ± 0.1 eV may be attributed to metallic Mg covered by the corroded film. The Mg present within the corrosion film predominantly existed as MgO, as confirmed by the single Mg 1s peak at BE = 1304.4 ± 0.1 eV. Based on the XPS analysis, the HA as well as $MgO/Mg(OH)_2$ may have formed on the sample surface during the immersion in Hank's solution, which is consistent with the XRD analysis shown in Fig. 12.

Antibacterial activity in vitro

To investigate the antibacterial behavior of the as-cast Mg-2Zn-0.2Ca-*x*Ag(*x* = 0, 0.1, 0.3, 0.5 wt.%) alloys, extract solutions were prepared and co-cultured with mixed suspensions of *Escherichia coli* and *Staphylococcus aureus* for 12 h, followed by plate spreading. The bacterial growth results are presented in Fig. 14(a–f). Compared with the negative control group, all Mg alloy extract solutions exhibited a noticeable reduction in bacterial colonies. Notably, the introduction of Ag markedly enhanced the antibacterial activity; the Ag-containing as-cast Mg-2Zn-0.2Ca alloys demonstrated significantly fewer bacterial colonies than the Ag-free ZX20 alloy. Fig. 14(g) summarizes the antibacterial rates of the different alloy extract solutions against *E. coli* and *S. aureus* after 12 h co-culture. The antibacterial rate of the Ag-free Mg-2Zn-0.2Ca alloy was only 61.38%. After the addition of 0.1 wt.% Ag, the antibacterial efficiency of ZXQ0.1 increased significantly ($p < 0.0001$), reaching 89.59%, which was even higher than that of the commercial WE43 alloy (positive control). With further Ag addition (0.3 wt.% and 0.5 wt.%), the antibacterial rate continued to increase, although the improvement margin narrowed, and both alloys achieved antibacterial rates exceeding 99%. The antibacterial capability of the extract solutions followed the order: ZX20< ZXQ0.1 < ZXQ0.3/ZXQ0.5, indicating a progressive enhancement of antibacterial activity with increasing Ag content.

To elucidate the underlying causes of the antibacterial differences among the alloy extracts, the pH values and ion concentrations in the extract solutions were analyzed. Fig. 15 presents the concentrations of Mg^{2+} and Ag^+ ions, as well as solution pH, after immersion of the alloys in Hank's solution for 72 h (Ca^{2+} concentrations were excluded due to non-significance in antibacterial contribution). As shown in Fig. 15(a), the Mg^{2+} concentration slightly increased from 81.8 ± 2.8 mg/L to 82.5 ± 1.3 mg/L after adding 0.1 wt.% Ag, although the difference was not statistically significant. In contrast, further Ag addition resulted in a remarkable increase in Mg^{2+} concentration ($p < 0.001$), reaching 95.0 ± 1.0 mg/L for ZXQ0.3 and 100.1 ± 3.7 mg/L for ZXQ0.5. The WE43 alloy exhibited the highest Mg^{2+} concentration (163.9 ± 6.1 mg/L). As shown in Fig. 15(b), the Ag^+ concentration in the ZXQ0.1 extract solution was 8.63 ± 1.39 μg/L. With increasing Ag content (0.3 and 0.5 wt.%), the Ag^+ concentration increased significantly ($p < 0.0001$) and reached a maximum value of 20.95 ± 2.18 μg/L in ZXQ0.5. In contrast, Zn^{2+} concentrations showed no statistical difference among the alloys (Fig. 15(c)). As presented in Fig. 15(d), the extract solution pH values remained approximately 11.1 for ZXQ0.1 and ZXQ0.3, and slightly increased to 11.2 ± 0.4 for ZXQ0.5, comparable to WE43, although the difference was not

ARTICLE IN PRESS

statistically significant.

Discussion

The corrosion behavior of the as-cast Mg-2Zn-0.2Ca-*x*Ag alloys in Hank's solution is governed by micro-galvanic coupling between the α-Mg matrix and the $Ca_2Mg_6Zn_3$ secondary phase, as well as the formation and evolution of surface corrosion products. Although trace Ag additions did not introduce new detectable intermetallic phases, EDS analysis confirmed progressive Ag enrichment within the $Ca_2Mg_6Zn_3$ grain-boundary phase. This compositional redistribution is expected to modify the electrochemical characteristics of the secondary phase. Specifically, Ag segregation increases the electrochemical nobility of the secondary phase relative to the α-Mg matrix, thereby enlarging the local potential difference between adjacent phases and altering the intensity of micro-galvanic coupling[23]. Microstructural characterization shows that discontinuously distributed $Ca_2Mg_6Zn_3$ phases are mainly located along grain boundaries, and Ag preferentially co-segregates into these phases without forming independent Ag-containing compounds, as shown in Fig. 3. Because these phases are distributed along grain boundaries, the galvanic interaction is spatially concentrated in these regions, leading to preferential anodic dissolution of the adjacent α-Mg matrix during immersion. The α-Mg matrix therefore acts as the anodic region and dissolves preferentially, while the secondary phases behave as local cathodes, resulting in localized pit initiation along grain boundaries (Fig. 10 and 11). The degradation of magnesium alloys in aqueous solution proceeds via the following electrochemical reactions:

Anodic dissolution

$$Mg \rightarrow Mg^{2+} + 2e^- \quad (1)$$

Cathodic hydrogen evolution

$$H_2O + 2e^- \rightarrow 2OH^- + H_2\uparrow \quad (2)$$

Formation of corrosion product

$$Mg^{2+} + 2H_2O \rightarrow Mg(OH)_2 + H_2\uparrow \quad (3)$$

Anodic dissolution produces Mg^{2+} and electrons, while cathodic hydrogen evolution generates OH^- and H_2 leading to a rapid increase in local pH, followed by the precipitation of $Mg(OH)_2$ and calcium–phosphate compounds. Such local alkalinization has been demonstrated to promote osteogenesis and mineralized matrix deposition; therefore, the alkaline microenvironment generated during Mg alloy degradation may provide a biologically favorable condition for peri-implant bone regeneration[47-50]. XRD and XPS analyses confirm that the corrosion products mainly consist of $Mg(OH)_2$ and hydroxyapatite (HA), forming a partially protective surface layer that temporarily retards pit propagation and suppresses further corrosion expansion (Fig. 12, Fig. 13). Magnesium is an essential micronutrient involved in cellular metabolism, membrane stability, and tissue homeostasis. The recommended dietary magnesium intake for adults is 280-360 mg/day for females and 350-420 mg/day for males, significantly higher than that of Fe (8-18 mg/day) or Zn (8-11 mg/day)[51]. As shown in Fig. 6, the Mg^{2+} release of the novel magnesium alloy in this study remained within a safe range. Notably, cells tolerate magnesium ion concentrations up to approximately 16 mmol/L, far exceeding physiological baseline levels[8,52]. Moreover, animal studies further revealed that excessive Mg^{2+} generated from degradable implants does not induce

ARTICLE IN PRESS

systemic toxicity, even in chronic renal insufficiency models[53], nor does it result in pathological deposition in lymph nodes after cranial implantation[54].

The effect of Ag on corrosion is highly concentration-dependent. An appropriate addition of Ag can refine secondary phases, optimize the cathode-to-anode area ratio, and suppress micro-galvanic corrosion, thereby improving corrosion resistance[30]. In Mg-Zn-Ca systems, the introduction of 0.3 wt.% Ag has been reported to promote grain refinement and homogenize precipitates, leading to enhanced corrosion resistance[26]. In the present study, at a low addition level (0.1 wt.%), Ag segregation remains limited, and the increase in cathodic nobility of the secondary phase is relatively small. As a result, the galvanic driving force between the grain-boundary phase and the α-Mg matrix is not significantly intensified. Under this condition, the corrosion behavior is more strongly influenced by the formation of a relatively compact and protective corrosion product layer, which contributes to improved film stability and slightly reduced degradation. Consequently, electrochemical measurements reveal that ZXQ0.1 exhibits the lowest corrosion current density and the highest polarization resistance, together with the largest Nyquist semicircle diameter (Fig. 5), indicating enhanced charge transfer resistance and improved stability of the surface product film. The lowest Mg^{2+} release and pH variation (Fig. 6) further confirm the suppressed degradation kinetics.

However, higher Ag content enhances micro-galvanic coupling with the Mg matrix and aggravates localized corrosion[27 35]. In the present study, further increasing Ag content (0.3-0.5 wt.%) led to greater Ag enrichment within the grain-boundary secondary phases, thereby strengthening their cathodic character and intensifying micro-galvanic coupling with the Mg matrix. This accelerates localized anodic dissolution adjacent to grain boundaries and aggravates localized corrosion. Consequently, corrosion current density increases by nearly one order of magnitude, while polarization resistance and EIS impedance decrease markedly (Fig. 5). Cross-sectional morphologies (Fig. 11) reveal deeper localized pits, consistent with the enhanced micro-galvanic attack. In addition, excessive Ag appears to destabilize the corrosion product film. Although thicker corrosion product layers are detected at higher Ag contents, these layers are more porous and prone to detachment. Frequent film breakdown exposes fresh Mg substrate, which further accelerates localized dissolution and promotes pit deepening resulting in destabilized films and reduced protective efficiency. This positive feedback between galvanic coupling and film instability explains the pronounced deterioration in corrosion resistance at 0.3-0.5 wt.% Ag.

Overall, the observed degradation trend of "initial improvement followed by deterioration" reveals a composition-dependent mechanistic link among Ag segregation, local electrochemical potential difference, film stability, and the resulting corrosion morphology and kinetics.

The antibacterial activity of Mg alloys is primarily attributed to the release of antibacterial ions during degradation and the resulting alkaline microenvironment. Local pH elevation (pH > 9) induced by Mg alloy degradation can contribute to bacterial inhibition by collapsing the proton electrochemical gradient and reducing bacterial surface hydrophobicity[55,56]. Rahim et al.[57] reported that bacterial proliferation was inhibited in Mg alloy extracts, with antibacterial activity increasing at higher pH values, whereas neutralization of the extract completely abolished the effect. However, it should be noted that elevated pH is not universally beneficial; excessive alkalization can disrupt

ARTICLE IN PRESS

cellular function, impair osteoblast activity, or even induce cell necrosis, underscoring the necessity of thorough cytocompatibility assessment. Accumulating evidence indicates that pH elevation alone cannot fully explain the composition-dependent differences in antibacterial efficacy observed among Mg-based alloys, with metal ion release and associated mechanisms playing important roles in governing antibacterial performance[58,59]. In the present study, the pH values of the different Mg-2Zn-0.2Ca-*x*Ag alloys were comparable, indicating that differences in antibacterial performance among the alloys cannot be attributed to pH variations.

The role of Mg^{2+} also remains controversial, with different studies reporting varying results. High Mg^{2+} concentrations have been reported to inhibit bacterial adhesion and biofilm formation, enhancing susceptibility to adverse conditions[60,61]. Yet, other studies found no correlation between Mg^{2+} concentration and antibacterial efficacy. Robinson et al.[62] and Liu et al.[63] observed negligible antibacterial effects from increased Mg^{2+} or pure Mg under neutral conditions. Consistently, in this study, although WE43 leachates contained the highest Mg^{2+} (Fig. 15), they did not exhibit the strongest antibacterial activity, confirming that Mg^{2+} is not the primary determinant. Similarly, Zn^{2+} levels in Mg-2Zn-0.2Ca-*x*Ag leachates did not vary significantly, suggesting that Zn^{2+} release is also not a key factor underlying antibacterial differences.

Statistically significant differences in Ag^{+} concentration were observed among the alloy groups, establishing a direct correlation between Ag incorporation and antibacterial performance. Although infection prevention within the first 48 h after implantation is clinically critical, antibacterial protection should not be limited to this initial period. Compared with surface coating strategies, alloying-based incorporation of Ag enables intrinsic antibacterial functionality that is synchronized with material degradation, thereby potentially providing more sustained antibacterial protection during degradation than short-lived surface-restricted strategies. The progressive increase in Ag^{+} concentration with increasing Ag content further indicates that compositional regulation effectively governs ion release during degradation, thereby dictating the biological response. The results suggest that Ag^{+} release is the dominant contributor. Ag^{+} ions disrupt bacterial membrane integrity, bind to thiol-containing proteins, and interfere with DNA replication, ultimately leading to bacterial cell death[64]. In addition, alkalization induced by Mg degradation may exert a synergistic inhibitory effect on bacterial growth. However, excessive alkalization could impair host cell viability, underscoring the need to balance antibacterial efficacy with cytocompatibility through controlled degradation and ion release.

Silver exhibits broad-spectrum antimicrobial activity at low concentrations (0.1 ng/mL-0.1 μg/mL)[65-67], and Mg-Ag alloys with appropriate Ag contents have been reported to show enhanced antibacterial performance together with acceptable biocompatibility with minimal cytotoxicity at antibacterial-relevant levels[56,68]. However, the biological effects are strongly dose-dependent: low Ag^{+} concentrations may provide effective antibacterial action without impairing osteoblast proliferation, whereas higher concentrations may induce cytotoxicity or exacerbate micro-galvanic corrosion. Previous studies have shown that high concentrations of AgNPs can inhibit cell proliferation[69] , whereas lower concentrations may support cell growth or exert adverse effects depending on the exposure conditions and cell type[70 71]. In addition, fibronectin-conjugated AgNPs at approximately 30 μg/mL have been reported to enhance proliferation, migration, and anti-

ARTICLE IN PRESS

inflammatory responses[72]. In the present study, Ag^+ concentrations in the alloy extracts remained below 30 μg/L (Fig. 15b), which is lower than concentration ranges commonly associated with obvious cytotoxicity[73]. These findings suggest that minor Ag additions may contribute to antibacterial efficacy while maintaining acceptable cytocompatibility under the present in vitro conditions, although direct cytocompatibility evaluation is still required.

Recent studies on Mg-based alloys have further shown that minor Ag incorporation can significantly enhance antibacterial efficacy through sustained Ag^+ release, with the antibacterial performance closely associated with Ag-induced changes in degradation behavior and ion-release characteristics[27,28,30,74]. Moreover, the interplay among degradation rate, pH evolution, Ag^+ release, and antibacterial activity has been increasingly recognized as a key factor in balancing corrosion regulation and antibacterial function[74].

In the present study, Ag^+ concentrations varied markedly with alloy composition. Correspondingly, antibacterial efficacy correlated strongly with Ag^+ levels: higher Ag content led to increased Ag^+ release and enhanced antibacterial performance (Fig. 14, Fig. 15). These results indicate that, although local alkalization and Mg^{2+}/Zn^{2+} release may provide supportive antibacterial effects, Ag^+ release is the dominant factor.

Given the well-known dose-dependent cytotoxicity of silver ions, direct cytocompatibility evaluation and systematic in vivo biosafety assessment are essential before any definitive conclusion regarding biosafety can be drawn. In the present study, antibacterial testing based on the extract method primarily reflects ion-mediated antibacterial effects and does not capture direct bacteria-surface interactions or biofilm-related behavior. In addition, although the measured Ag^+ concentrations were relatively low, long-term in vivo studies are still required to assess the potential systemic fate and accumulation of released silver during degradation.

The corrosion behavior and antibacterial performance of Mg-2Zn-0.2Ca-*x*Ag alloys are closely linked through degradation-driven ion release and surface reactions. A moderate corrosion rate helps maintain a relatively stable local environment and supports sustained ion availability, which favors both biocompatibility and antibacterial effectiveness. In the present study, Ag addition showed a concentration-dependent effect: 0.1 wt.% Ag facilitated the formation of a more stable corrosion product layer while still providing sufficient Ag^+ release for effective antibacterial action, whereas further increasing the Ag content intensified micro-galvanic corrosion and impaired film stability. Among all the investigated alloys, ZXQ0.1 (Mg-2Zn-0.2Ca-0.1Ag) exhibited the most balanced overall performance, combining the lowest corrosion rate with significantly improved antibacterial activity. These findings demonstrate that precise regulation of Ag content is critical for balancing corrosion stability and antibacterial functionality, and identify ZXQ0.1 as a promising candidate for biodegradable implant applications.

Methods

Sample preparation and characterization

The alloys with designed compositions were prepared through conventional melting and vertical DC casting technique. High-purity Mg ingots (99.95 wt.%), Zn granules (99.99 wt.%), a Mg-25 wt.% Ca master alloy, and Ag billets (99.99 wt.%) were used as feeding materials for

ARTICLE IN PRESS

melting. The alloys were melted in a steel crucible under argon protection, subsequently refined, and cast under a CO_2 + SF_6 shielding gas mixture at 680 °C using a vertical DC casting technique with a casting speed of around 80 mm/min to produce cylindrical billets with a diameter of 140 mm. The Mg-2Zn-0.2Ca-*x*Ag (*x* = 0, 0.1, 0.3, 0.5 wt.%) alloys investigated in this study were fabricated according to the designed compositions. The actual chemical compositions were determined by ICP-OES (Spectro Blue Sop, Germany) in our previous work and were found to be consistent with the nominal compositions. The detailed measured compositions have been reported in our previous study[23].

Specimens with dimension of 10 mm × 10 mm × 50 mm were machined directly from the as-cast ingots for immersion and electrochemical tests, while plates measuring 20 mm × 20 mm × 10 mm were prepared for extract preparation. Prior to the designated tests, all samples were ground using SiC abrasive papers, followed by ultrasonic cleaning in ethanol and deionized water, and then air-dried. The samples intended for extract preparation were subsequently sterilized using low-temperature hydrogen peroxide plasma (LK/MJQ-100, Chengdu Laoken Medical Technology Co., Ltd., China) in standard mode (maximum temperature 57.3 °C; maximum chamber pressure 170 Pa) before biological testing to ensure sterility while minimizing potential surface alterations, as hydrogen peroxide gas plasma sterilization has been demonstrated to preserve surface integrity and material properties in medical devices[75,76].

Metallographic observation was performed using an optical microscopy (OM, Olympus BX51M, Japan). Microstructural and compositional features were further characterized using SEM (Tescan Mira3, Czech Republic) equipped with an EDS detector. Phase constitution was assessed using X-ray diffraction (XRD, Rigaku D/MAX-2500VB, Japan) within a 2θ range of 20°-80° at a scan rate of 1°/min (Cu Kα radiation). SEM/EDS were used to characterize the surface corrosion morphology and cross-sectional features after 168 h of immersion, whereas three-dimensional corrosion topography was obtained by optical tomography after 14 d of immersion. To further identify the corrosion products, XRD (10°-90°) and XPS (Thermo ESCALAB 250Xi) analyses were performed after 28 d of immersion. The binding energies in the XPS spectra were calibrated using the C 1s peak at 284.8 eV as the reference.

Electrochemical corrosion tests

The corrosion resistance of the samples was evaluated using open circuit potential (OCP), potentiodynamic polarization curves (PDP) and electrochemical impedance spectroscopy (EIS), conducted with a CS310 workstation (China) in Hank's solution (Biosharp, BL561A) at 37 ± 1 ºC. The solution contained NaCl 8.00 g L^{-1}, glucose 1.00 g L^{-1}, KCl 0.40 g L^{-1}, $NaHCO_3$ 0.35 g $^{-1}$, $CaCl_2$ 0.14 g L^{-1}, $MgCl_2 \cdot 6H_2O$ 0.10 g L^{-1}, $MgSO_4 \cdot 7H_2O$ 0.06 g L^{-1}, $Na_2HPO_4 \cdot 12H_2O$ 0.06 g L^{-1}, and KH_2PO_4 0.06 g L^{-1}. A three-electrode cell was employed, consisting of a saturated calomel reference electrode, a counter electrode made of Pt foil, and the specimen serves as the working electrode. The surface area exposed to the corrosive electrolyte was 1 cm^2. Potentiodynamic polarization was performed after the OCP had stabilized, and the potential was scanned from -0.3 V to +0.3 V *vs.* OCP at a rate of 1 mV/s. The corrosion current density (i_{corr}) was estimated by approximate extrapolation of the relatively stable quasi-linear cathodic branch near E_{corr}, because no reliable linear anodic Tafel region was observed. The fitting region was selected from the

ARTICLE IN PRESS

cathodic segment close to E_{corr} while avoiding portions showing obvious curvature or instability. The fitted cathodic Tafel slope (β_c) was obtained from this linear region. Since the cathodic quasi-linear region was limited in extent, the obtained i_{corr} values were used primarily as comparative electrochemical indicators to assess the relative corrosion tendency among the alloys. Corrosion rate *Pi* (mm/year) was calculated as:

$$P_i = 22.85\ i_{corr} \quad (4)$$

In vitro degradation evaluation

Corrosion behavior was evaluated in Hank's solution (Biosharp, BL561A) following ASTM G31-72[41]. The solution volume-to-surface area ratio was maintained at 20 mL/cm², and tests were conducted at 37 ± 0.5 °C for 168 h and 672h. During 168 hours' immersion, pH was measured using a calibrated digital pH meter (PHS-3C, Leici, China). Mg^{2+} concentration was quantified by ICP-OES (Spectro Blue Sop, Germany). After immersion, corrosion products were removed by rinsing the samples using 200 g/L CrO_3 solution for 10 min, and the corrosion rates (mm/year) were calculated using:

$$P_w = \frac{K \times \Delta W}{A \times t \times D} \quad (5)$$

Where $K = 8.76 \times 10^4$; ΔW = weight loss (g); A = exposed surface area (cm^2); t = immersion time (h); D = alloy density (g/cm^3). The experiment was repeated three times to ensure data reliability.

In-vitro Antibacterial Activity

Extract solutions were prepared according to ISO 10993-12 guidelines[77]. Sterilized samples were immersed in Hank's solution at a surface-area-to-volume ratio of 1.25 cm^2/ 1 mL and incubated at 37 °C for 72 h. The solutions were centrifuged (3000 rpm, 5 min), and supernatants were collected and stored at 4 °C. The pH of the extracts was recorded (PHS-3C, Leici, China), and concentrations of released Mg^{2+}, Ca^{2+}, Zn^{2+} and Ag^{+} were quantified using ICP-OES (Spectro Blue Sop, Germany) and ICP-MS (NexION 2000, PerkinElmer, USA).

Escherichia coli (*E. coli ATCC 25922*) and *Staphylococcus aureus* (*S. aureus ATCC 29213*) were selected to evaluate the in vitro antibacterial properties of various Mg alloys. The two strains were mixed at a 1:1 ratio to assess the overall antibacterial effect of the alloy extracts in a dual-species bacterial system. This mixed-culture model was adopted to better reflect a polymicrobial environment relevant to implant-associated infection[78]. Revived strains were cultured on TSA plates (BD Difco, 236950) at 37 °C for 24 h, followed by incubation in LB broth (Miller's, 12795027) at 37 °C and 120 rpm to obtain logarithmic-phase suspensions. Bacterial suspensions were adjusted to ~10^7 CFU/mL, and alloy extracts were used for antibacterial assessment. Briefly, 100 µL bacterial suspension, 250 µL extract, and 650 µL LB medium were co-incubated at 37 °C, 5% CO_2 for 12 h; Hank's solution served as control. Suspensions were serially diluted, plated, incubated for 12 h, and colonies (30-300 CFU) were counted according to GB 4789.2-2016**.** Antibacterial rate was calculated as:

$$Antibacterial\ rate(\%) = \left(1 - \frac{N_x}{N_b}\right) \times 100\% \quad (6)$$

Where (N_x) and (N_b) represent the number of colonies on the experimental and control plates,

ARTICLE IN PRESS

respectively. The experiment was repeated three times to ensure data reliability.

Statistical Methods

Data were presented as mean values ± standard deviation. Statistical analyses were conducted using SPSS 21, and intergroup differences were evaluated using one-way ANOVA followed by Tukey's post-hoc test. Differences of p-values < 0.05 were considered statistically significant.

Data availability

The datasets generated and/or analyzed during the current study are not publicly available as the analysis is part of an ongoing larger project and future publications are planned. However, they are available from the corresponding author on reasonable request.

Acknowledgements

This work was supported by the Natural Science Foundation of Hunan Province Joint Fund for the Medical and Health Sector (Grant No. 2025JJ80899) and the Hunan Provincial Natural Science Foundation of China (Grant No. 2023JJ40920).

Author contributions

Fang Yi contributed to data acquisition, analysis, and interpretation of the experiments and drafted the manuscript. Meng-Zhi Wu and Jing Guo conducted and contributed to antibacterial tests and data acquisition. Yi Chen contributed to the analysis of electrochemical characterization data**.** Lingzhi Yang contributed to the analysis of XPS spectra. Yonghao Gao contributed to the design, analysis, and interpretation of corrosion and electrochemical characterization tests, and participated in manuscript revision. All authors have read and approved the final manuscript**.**

Competing interests

The authors declare no competing financial or non-financial interests.

ARTICLE IN PRESS

References

1 Luo, Y. *et al.* Update on the research and development of magnesium-based biodegradable implants and their clinical translation in orthopaedics. *BMT* **2**

2 Chen, Y. J. *et al.* Recent advances on the development of magnesium alloys for biodegradable implants. *Acta Biomaterialia* **10**, 4561-4573.

3 Cousin, A. S. *et al.* Severity and long-term complications of surgical site infections after orthognathic surgery: a retrospective study. *Scientific Reports* **10**

4 Xing, F. *et al.* Recent progress in Mg-based alloys as a novel bioabsorbable biomaterials for orthopedic applications. *Journal of Magnesium and Alloys* **10**, 1428-1456.

5 Wang, B. *et al.* Incidence and Risk Factors of Infection After Fracture Fixation: A Multicenter Cohort Study. *Orthop Surg* **17**, 151-162.

6 Morgenstern, M. *et al.* Diagnostic challenges and future perspectives in fracture-related infection. *Injury-International Journal of the Care of the Injured* **49**, S83-S90.

7 Niu, E. C. *et al.* Controllable degradation behavior, mechanical properties and biocompatibility of Mg-Sr-Mn alloys for the orthopedic medical applications. *Npj Materials Degradation* **9**

ARTICLE IN PRESS

8 Xia, D. D. *et al.* Research status of biodegradable metals designed for oral and maxillofacial applications: A review. *Bioactive Materials* **6**, 4186-4208.

9 Istrate, B. *et al.* Current Research Studies of Mg-Ca-Zn Biodegradable Alloys Used as Orthopedic Implants-Review. *Crystals* **12**

10 Wang, L. *et al.* Review: Degradable Magnesium Corrosion Control for Implant Applications. *Materials (Basel)* **15**

11 Li, Y. *et al.* Controllable degradation behavior of Mg-Sr-Y alloys for the bio-applications. *npj Materials Degradation* **7**, 45.

12 Tong, X. *et al.* Enhanced Mechanical Properties, Corrosion Resistance, Cytocompatibility, Osteogenesis, and Antibacterial Performance of Biodegradable Mg-2Zn-0.5Ca-0.5Sr/Zr Alloys for Bone-Implant Application. *Adv Healthc Mater* **13**, e2303975.

13 Mozaffari, F. Microstructure, mechanical properties and bio-corrosion behavior of Mg–2Zn-0.3Ca-x (x= 0, 0.5, 1.0) Y alloys. *Journal of materials research and technology* **31**, 1017-1027.

14 Nan, J. *et al.* Research on the antibacterial properties of nanoscale zinc oxide particles comprehensive review. *Frontiers in Materials* **Volume 11 - 2024**

15 Sahu, M. R. *et al.* An overview of the recent developments in biodegradable Mg-Zn alloy. *Journal of Magnesium and Alloys* **13**, 486-509.

16 Guo, F. *et al.* Microstructure and texture in an extruded Mg–Al–Ca–Mn flat-oval tube. *Journal of Magnesium and Alloys* **5**, 13-19.

17 Du, Y. *et al.* Corrosion behavior of a Mg-Zn-Ca-La alloy in 3.5 wt% NaCl solution. *Journal of Magnesium and Alloys* **10**, 527-539.

18 Liu, X. *et al.* Effect of micro-alloying Ca on microstructure, texture and mechanical properties of Mg-Zn-Y-Ce alloys. *Progress in Natural Science-Materials International* **30**, 213-220.

19 Qu, Y. *et al.* Evaluation of a new Mg-Zn-Ca-Y alloy for biomedical application. *Journal of Materials Science-Materials in Medicine* **26**

20 Ma, Y.-z. *et al.* Microstructure, mechanical, and corrosion properties of extruded low-alloyed Mg-*x*Zn-0.2Ca alloys. *International Journal of Minerals Metallurgy and Materials* **26**, 1274-1284.

21 Ding, H. *et al.* Texture weakening and ductility variation of Mg–2Zn alloy with CA or RE addition. *Materials Science and Engineering: A* **645**, 196-204.

22 Zareian, Z. *et al.* Tailoring the mechanical properties of Mg–Zn magnesium alloy by calcium addition and hot extrusion process. *Materials Science and Engineering: A* **774**, 138929.

23 Yin, J. *et al.* Effects of micro-alloying Ag on microstructure, mechanical properties and corrosion behavior of extruded Mg-2Zn-0.2 Ca-xAg alloys. *Journal of Alloys and Compounds* **989**, 174376.

24 Zhang, C. *et al.* Antimicrobial Bioresorbable Mg-Zn-Ca Alloy for Bone Repair in a Comparison Study with Mg-Zn-Sr Alloy and Pure Mg. *ACS Biomater Sci Eng* **6**, 517-538.

25 Shao, Y. *et al.* Advance in Antibacterial Magnesium Alloys and Surface Coatings on Magnesium Alloys: A Review. *Acta Metallurgica Sinica (English Letters)* **33**, 615-629.

26 Yu, L. *et al.* The mechanical and corrosion resistance of Mg-Zn-Ca-Ag alloys: the influence of Ag content. *Journal of Materials Research and Technology-Jmr&T* **9**, 10863-10875.

27 Wang, X. *et al.* Effects of Ga/Ag addition on corrosion behavior, cytotoxicity, and antibacterial activity of biodegradable Mg–2Zn alloy. *Journal of Materials Research and Technology* **29**, 3144-3155.

ARTICLE IN PRESS

28 Razzaghi, M. *et al.* In Vitro Degradation, Antibacterial Activity and Cytotoxicity of Mg-3Zn-xAg Nanocomposites Synthesized by Mechanical Alloying for Implant Applications. *Journal of Materials Engineering and Performance* **28**, 1441-1455.

29 Razzaghi, M. *et al.* Microstructure, mechanical properties, and in-vitro biocompatibility of nano- NiTi reinforced Mg–3Zn-0.5Ag alloy: Prepared by mechanical alloying for implant applications. *Composites Part B: Engineering* **190**, 107947.

30 Ma, Y.-z. *et al.* Microstructure, mechanical properties and corrosion behavior of quaternary Mg-1Zn-0.2Ca-*x*Ag alloy wires applied as degradable anastomotic nails. *Transactions of Nonferrous Metals Society of China* **31**, 111-124.

31 Zhao, H. *et al.* Microstructure, Mechanical Properties and Corrosion Behavior of Extruded Mg-Zn-Ag Alloys with Single-Phase Structure. *Acta Metallurgica Sinica-English Letters* **31**, 575-583.

32 Nie, Y. J. *et al.* Effect of Ag Addition on Microstructure, Mechanical and Corrosion Properties of Mg-Nd-Zn-Zr Alloy for Orthopedic Application. *Acta Metallurgica Sinica-English Letters* **36**, 295-309.

33 Guo, C. *et al.* Influence of Zn and/or Ag additions on microstructure and properties of Al-Mg based alloys. *Journal of alloys and compounds* **904**, 163998.

34 Zhang, D.-d. *et al.* Effects of trace Ag on precipitation behavior and mechanical properties of extruded Mg-Gd- Y-Zr alloys. *Transactions of Nonferrous Metals Society of China* **31**, 3394-3404.

35 Asadollahi, M. *et al.* Toward understanding the effects of solution heat treatment, Ag addition, and simultaneous Ag and Cu addition on the microstructure, mechanical properties, and corrosion behavior of the biodegradable Mg-2Zn alloy. *Journal of Materials Research and Technology-Jmr&T* **26**, 1553-1571.

36 Yang, L. *et al.* Effect of Ag on cathodic activation and corrosion behaviour of Mg-Mn-Ag alloys. *Corrosion Science* **185**, 109408.

37 Dragomir, L. *et al.* Microstructure and corrosion behaviour of Mg-Ca and Mg-Zn-Ag alloys for biodegradable hard tissue implants. *Crystals* **13**, 1213.

38 Yi, F. *et al.* In-vitro corrosion and mechanical degradation of Mg-2Zn-0.2Ca-xAg alloys in Hanks' solution. *Journal of Alloys and Compounds* **1057**, 186770.

39 Zhu, T. *et al.* Effect of Initial Orientation on Corrosion Behavior of AZ80 Magnesium Alloy in Simulated Body Fluid. *Metals and Materials International* **27**, 2645-2655.

40 Prince, L. *et al.* Inhibitive effect of sodium carbonate on corrosion of AZ31 magnesium alloy in NaCl solution. *Corrosion Science* **179**, 109131.

41 Chen, H. *et al.* Corrosion behavior of in-situ synthesized ZnO-containing coatings of AZ31B magnesium alloy by micro-arc oxidation in simulated body fluids. *Chemistryselect* **9**

42 Zhang, Y. *et al.* Influence of Uric Acid on the Corrosion Behavior of AZ31 Magnesium Alloy in Simulated Body Fluid. *Journal of Materials Engineering and Performance*

43 Vaidhyanathan, B. *et al.* Fabrication and Investigation of the Suitability of Chitosan-Silver Composite Scaffolds for Bone Tissue Engineering Applications. *Process Biochemistry* **100**, 178-187.

44 Wang, L. Q. *et al.* Insight into physical interpretation of high frequency time constant in electrochemical impedance spectra of Mg. *Corrosion Science* **187**

45 Raikar, G. N. *et al.* Hydroxyapatite Characterized by XPS. *Surface Science Spectra* **4**, 9-13.

46 Pelavin, M. *et al.* Phosphorus 2p electron binding energies. Correlation with extended Hueckel charges. *The Journal of Physical Chemistry* **74**, 1116-1121.

ARTICLE IN PRESS

47 Galow, A.-M. *et al.* Increased osteoblast viability at alkaline pH in vitro provides a new perspective on bone regeneration. *Biochemistry and biophysics reports* **10**, 17-25.

48 Shen, Y. H. *et al.* Interfacial pH: A Critical Factor for Osteoporotic Bone Regeneration. *Langmuir* **27**, 2701-2708.

49 Subrahmanyam, D. K. S. *et al.* Wilson's disease - A rare cause of renal tubular acidosis with metabolic bone disease. *Indian journal of nephrology* **24**, 171-174.

50 Liu, W. *et al.* Akermanite used as an alkaline biodegradable implants for the treatment of osteoporotic bone defect. *Bioactive materials* **1**, 151-159.

51 Razzaque, M. S. *et al.* Minerals and Human Health: From Deficiency to Toxicity. *Nutrients* **17**

52 Xia, D. *et al.* Research status of biodegradable metals designed for oral and maxillofacial applications: A review. *Bioactive Materials* **6**, 4186-4208.

53 Wang, J. *et al.* Biodegradable Magnesium (Mg) Implantation Does Not Impose Related Metabolic Disorders in Rats with Chronic Renal Failure. *Scientific Reports* **6**, 26341.

54 Torroni, A. *et al.* Biocompatibility and degradation properties of WE43 Mg alloys with and without heat treatment: In vivo evaluation and comparison in a cranial bone sheep model. *Journal of Cranio-Maxillofacial Surgery* **45**, 2075-2083.

55 Ikeuba, A. I. Bimetallic corrosion evaluation of the ?-Al8Mg3FeSi6 phase/Al couple in acidic, neutral and alkaline aqueous solutions using the scanning vibrating electrode technique. *Electrochimica Acta* **449**

56 Lin, Z. S. *et al.* The Role of Antibacterial Metallic Elements in Simultaneously Improving the Corrosion Resistance and Antibacterial Activity of Magnesium Alloys. *Materials & Design* **198**

57 Rahim, M. I. *et al.* Alkalization is responsible for antibacterial effects of corroding magnesium. *Journal of Biomedical Materials Research Part A* **103**, 3526-3532.

58 Wang, N. *et al.* Mg-, Zn-, and Fe-Based Alloys With Antibacterial Properties as Orthopedic Implant Materials. *Frontiers in Bioengineering and Biotechnology* **Volume 10 - 2022**

59 Song, Q. *et al.* Antibacterial Pure Magnesium and Magnesium Alloys for Biomedical Materials—A Review. *Crystals* **14**, 939.

60 Demishtein, K. *et al.* Antimicrobial Properties of Magnesium Open Opportunities to Develop Healthier Food. *Nutrients* **11**

61 Rodríguez-Sánchez, J. *et al.* Bactericidal effect of magnesium ions over planktonic and sessile *Staphylococcus epidermidis* and *Escherichia coli*. *Materials Chemistry and Physics* **221**, 342-348.

62 Robinson, D. A. *et al.* In vitro antibacterial properties of magnesium metal against Escherichia coli, Pseudomonas aeruginosa and Staphylococcus aureus. *Acta Biomaterialia* **6**, 1869-1877.

63 Liu, C. *et al.* Biodegradable Mg-Cu alloys with enhanced osteogenesis, angiogenesis, and long-lasting antibacterial effects. *Scientific Reports* **6**

64 Eltarahony, M. M. *et al.* Comparative antibacterial and anti-virulence effects of silver ions from electrolysis, silver nanoparticles, and silver nitrate against Pseudomonas aeruginosa and Staphylococcus aureus. *Scientific Reports* **16**, 4385.

65 Zhang, E. L. *et al.* Antibacterial metals and alloys for potential biomedical implants. *Bioactive Materials* **6**, 2569-2612.

66 Qin, Z. *et al.* Versatile roles of silver in Ag-based nanoalloys for antibacterial applications. *Coordination Chemistry Reviews* **449**, 214218.

ARTICLE IN PRESS

ARTICLE IN PRESS

67 Hao, Z. *et al.* Synergistic antibacterial mechanism of silver-copper bimetallic nanoparticles. *Frontiers in Bioengineering and Biotechnology* **11**, 1337543.

68 Damle, A. *et al.* A concise review on implications of silver nanoparticles in bone tissue engineering. *Biomaterials Advances* **141**

69 Greulich, C. *et al.* Studies on the biocompatibility and the interaction of silver nanoparticles with human mesenchymal stem cells (hMSCs). *Langenbeck's Archives of Surgery* **394**, 495-502.

70 Castiglioni, S. *et al.* Silver Nanoparticles in Orthopedic Applications: New Insights on Their Effects on Osteogenic Cells. *Nanomaterials* **7**, 124.

71 Jung, S. K. *et al.* Silver Nanoparticle–Induced hMSC Proliferation Is Associated with HIF-1α-Mediated Upregulation of IL-8 Expression. *Journal of Investigative Dermatology* **134**, 3003-3007.

72 Hung, H.-S. *et al.* Anti-Inflammatory Fibronectin-AgNP for Regulation of Biological Performance and Endothelial Differentiation Ability of Mesenchymal Stem Cells. *International Journal of Molecular Sciences* **22**, 9262.

73 Wu, J. *et al.* In vitro cytotoxicity of Cu^{2+}, Zn^{2+}, Ag^{+} and their mixtures on primary human endometrial epithelial cells. *Contraception* **85**, 509-518.

74 Ouyang, S. *et al.* More than the barrier effect: Biodegradable Mg-Ag alloy membranes for guided bone/tissue regeneration. *Journal of Magnesium and Alloys* **12**, 4454-4467.

75 Kocijan, A. *et al.* The Influence of Plasma Treatment on the Corrosion and Biocompatibility of Magnesium. *Materials (Basel)* **15**

76 Förtsch, M. *et al.* H_2O_2 low temperature plasma sterilization. New possibilities for use with eye surgery instruments. *Ophthalmologe* **90**, 754-764.

77 Heise, T. *et al.* Report on investigation of ISO 10993–12 extraction conditions. *Regulatory Toxicology and Pharmacology* **131**, 105164.

78 Sekar, A. *et al.* Characterizing interactions of Staphylococcus aureus and Escherichia coli in dual-species implant-associated biofilms. *npj Biofilms and Microbiomes* **11**, 189.

ARTICLE IN PRESS

Figure legends

Figure 1. Optical microstructure of the as-cast alloys. (a) ZX20, (b) ZXQ0.1, (c) ZXQ0.3, and (d) ZXQ0.5.

Figure 2. Second dendrite arm spacing and volume fraction of secondary phases (recrystallization) of the as-cast Mg-2Zn-0.2Ca-*x*Ag alloys.

(a) Second dendrite arm spacing, (b) volume fraction of secondary phases.

Figure 3. Microstructure of the as-cast alloys.

(a)-(d) show SEM images of the as-cast alloys: (a) ZX20, (b) ZXQ0.1, (c) ZXQ0.3, and (d) ZXQ0.5. In (a)-(d), red crosses and red numbers indicate selected EDS analysis positions, and yellow horizontal lines indicate the paths used for line-scan analysis. The corresponding elemental maps displayed to the right of each SEM image show the distributions of Mg, Zn, Ca, and Ag. (e)-(h) show the corresponding line-scan profiles of ZX20, ZXQ0.1, ZXQ0.3, and ZXQ0.5, respectively, obtained along the yellow horizontal lines marked in (a)-(d).

Figure 4. XRD patterns of the as-cast Mg-2Zn-0.2Ca-*x*Ag alloys.

Figure 5. Electrochemical behavior of the as-cast Mg-2Zn-0.2Ca-*x*Ag alloys.

(a) The open circuit potential, (b) Potentiodynamic polarization curves, (c) Nyquist plots, and (d) Bode plots. Electrochemical tests were performed after immersion of the alloys in Hank's solution at 37 °C for 12 h. The

ARTICLE IN PRESS

potentiodynamic polarization curves were measured from -0.3 V to +0.3 V versus OCP at a scan rate of 1 mV/s.

Figure 6. Weight loss test results and associated solution changes of the as-cast Mg-2Zn-0.2Ca-*x*Ag alloys.
(a) Corrosion rate, (b) mass loss rate, (c) pH value, and (d) Mg^{2+} concentration measured at different time points during immersion in Hank's solution over 168 h.

Figure 7. Optical macroscopic morphologies of the as-cast Mg-2Zn-0.2Ca-*x*Ag alloys.
This figure shows the optical macroscopic images of the surfaces of the as-cast Mg-2Zn-0.2Ca-*x*Ag alloys after immersion in Hank's solution for different times up to 168 h.

Figure 8. Fraction of the sample surface attacked by corrosion.
This parameter was measured at different time points during immersion in Hank's solution at 37 ± 1 °C over 168 h.

Figure 9. 3D tomographic maps of the as-cast alloys.
(a)-(d) show the 3D corrosion penetration of the alloys after 14 days of immersion in Hank's solution: (a) ZX20, (b) ZXQ0.1, (c) ZXQ0.3, (d) ZXQ0.5. (e) shows the corresponding corrosion depth profiles along selected lines.

Figure 10. Surface corrosion morphologies of the as-cast alloys.
This figure shows SEM images with and without corrosion products of the as-cast Mg-2Zn-0.2Ca-*x*Ag (*x*=0, 0.1, 0.3, 0.5 wt.%) alloys after immersion in Hank's solution for 168 hours. In each column's right image is an enlarged view of the area indicated by the yellow arrow in the left image.

Figure 11. Cross-sectional corrosion morphologies of the as-cast alloys.
(a)-(d) show the cross-sectional corrosion morphologies of the as-cast Mg-2Zn-0.2Ca-*x*Ag alloys after immersion in Hank's solution for 168 h: (a) ZX20, (b) ZXQ0.1, (c) ZXQ0.3, (d) ZXQ0.5. The red dashed lines and red numbers indicate the measured corrosion depth. (e) and (f) show higher-magnification cross-sectional SEM images of ZX20 and ZXQ0.3 respectively, and the corresponding elemental maps of representative corroded regions.

Figure 12. XRD patterns of the surface corrosion product films on the as-cast alloys.
XRD patterns were obtained from the surface corrosion product films after 28 days of immersion in Hank's solution at 37 ± 1 °C.

Figure 13. High-resolution XPS spectra of the as-cast alloys after immersion.
(a), (c), (e), (g), and (i) show the high-resolution XPS spectra of C, Mg, O, P, and Ca, respectively, for ZX20 after 28 days of immersion in Hank's solution. (b), (d), (f), (h), and (j) show the corresponding high-resolution XPS spectra of C, Mg, O, P, and Ca, respectively, for ZXQ0.5 after 28 days of immersion in Hank's solution.

Figure 14. Antibacterial activity of extracts from the as-cast alloys.
(a)-(f) show representative bacterial colonies on agar plates formed after 12 h co-culture of *E. coli* and *S. aureus* with diluted extracts of the as-cast Mg-2Zn-0.2Ca-*x*Ag alloys: (a) control, (b) ZX20, (c) ZXQ0.1, (d) ZXQ0.3, (e) ZXQ0.5, and (f) WE43. The extracts were diluted 100 times before plating. (g) shows the corresponding antibacterial rates. n=3, *p<0.05, **p<0.01, ***p<0.001, ****p<0.0001.

Figure 15. Ionic concentrations and pH values in the extracts of the as-cast alloys.
(a, b, c) concentrations of Mg^{2+}, Ag^{+} and Zn^{2+} ions and (d) the pH values in the extracts of the as-cast Mg-2Zn-0.2Ca-*x*Ag alloys. n=3, *p<0.05, **p<0.01, ***p<0.001, ****p<0.0001.

ARTICLE IN PRESS

Table 1. EDS results (at. %) of the selected points shown in Fig. 3.

Element	ZX20			ZXQ0.1			ZXQ0.3			ZXQ0.5		
	1#	2#	3#	4#	5#	6#	7#	8#	9#	10#	11#	12#
Mg	85.2	85.3	99.1	77.8	81.9	99.2	84.4	89.7	98.7	76.6	77.6	99.4
Zn	10.8	11.5	0.9	15.6	12.5	0.8	11	7.5	1.3	16.9	17.1	0.6
Ca	4.0	3.2	0	6.6	5.6	0	4.6	2.8	0	6.5	5.3	0
Ag	0	0	0	0.4	0.5	0	0.8	0.6	0	2.0	2.5	0

Table 2. Electrochemical data obtained via the Tafel fitting of PDP curves.

Samples	E_{corr} (V vs SCE)	i_{corr} (μA/cm^2)	βc (mV/decade)	P_i (mm/year)
ZX20	-1.53±0.01	1.99±0.33	-224.41±5.16	0.05±0.01
ZXQ0.1	-1.52±0.03	1.77±0.67	-221.58±19.95	0.04±0.02
ZXQ0.3	-1.51±0.05	4.80±0.93	-297.55±18.32	0.21±0.17
ZXQ0.5	-1.48±0.08	13.41±1.56	-205.25±38.59	0.31±0.04

Table 3. Electrochemical data obtained from the equivalent circuit fitting of EIS curves.

Samples	R_s /Ω·cm^2	R_{ct} /Ω·cm^2	CPE_{dl}-T /μF·s^{n-1}·cm^{-2}	CPE_{dl}-P	R_f /Ω·cm^2	CPE_f-T /μF·s^{n-1}·cm^{-2}	Rp /Ω·cm^2	CPE_f-P	R /Ω·cm^2	L /MH cm^{-2}	χ^2
ZX20	2.15	588.1	13.2	0.66	12270	4.78	12858.1	0.89	1	3.97	0.003
ZXQ0.1	2.45	529.0	10.4	0.68	16985	4.28	17514.0	0.91	1	3.40	0.003
ZXQ0.3	2.12	13.7	13.4	0.73	1252	77.2	1265.7	0.77	-	-	0.001
ZXQ0.5	1.96	16.7	49.7	0.55	1091	44.4	1107.7	0.78	1	0.23	0.003

Table 4. Corrosion rate and the mass loss of the as-cast alloys.

Samples	168 h		672 h	
	Corrosion rate	Mass loss	Corrosion rate	Mass loss
	(mm/y)	(%)	(mm/y)	(%)
ZX20	0.127±0.031	0.213±0.045	0.635±0.095	3.713±0.680
ZXQ0.1	0.121±0.016	0.208±0.032	0.560±0.145	3.744±1.100
ZXQ0.3	0.223±0.045	0.389±0.086	0.660±0.083	4.346±0.458
ZXQ0.5	0.232±0.029	0.370±0.038	0.745±0.09	4.985±0.615

ARTICLE IN PRESS

Table 5. EDS results (at. %) of the marked points in Fig. 10.

Element	ZX20		ZXQ0.1		ZXQ0.3		ZXQ0.5	
	1#	2#	3#	4#	5#	6#	7#	8#
C	19.3	16.3	12.9	27.6	3.9	18.8	13.8	10.9
O	57.2	59.3	55	37.6	52.3	49.1	53.6	43.5
Na	1.4	0.8	0.5	0.5	1.1	0.7	0.1	0
Mg	5.9	7.1	5.5	16.8	12	6.6	5.5	29.2
P	7.6	7	11.4	7.4	13	10.8	11.5	0
Ca	8.5	9.1	14.2	9.4	16.8	13.7	15.1	0.4
Cl	0.1	0.2	0.3	0.2	0.4	0	0.4	15.8
Zn	0.1	0.1	0.1	0.3	0.3	0.1	0	0.2

ARTICLE IN PRESS

ARTICLE IN PRESS

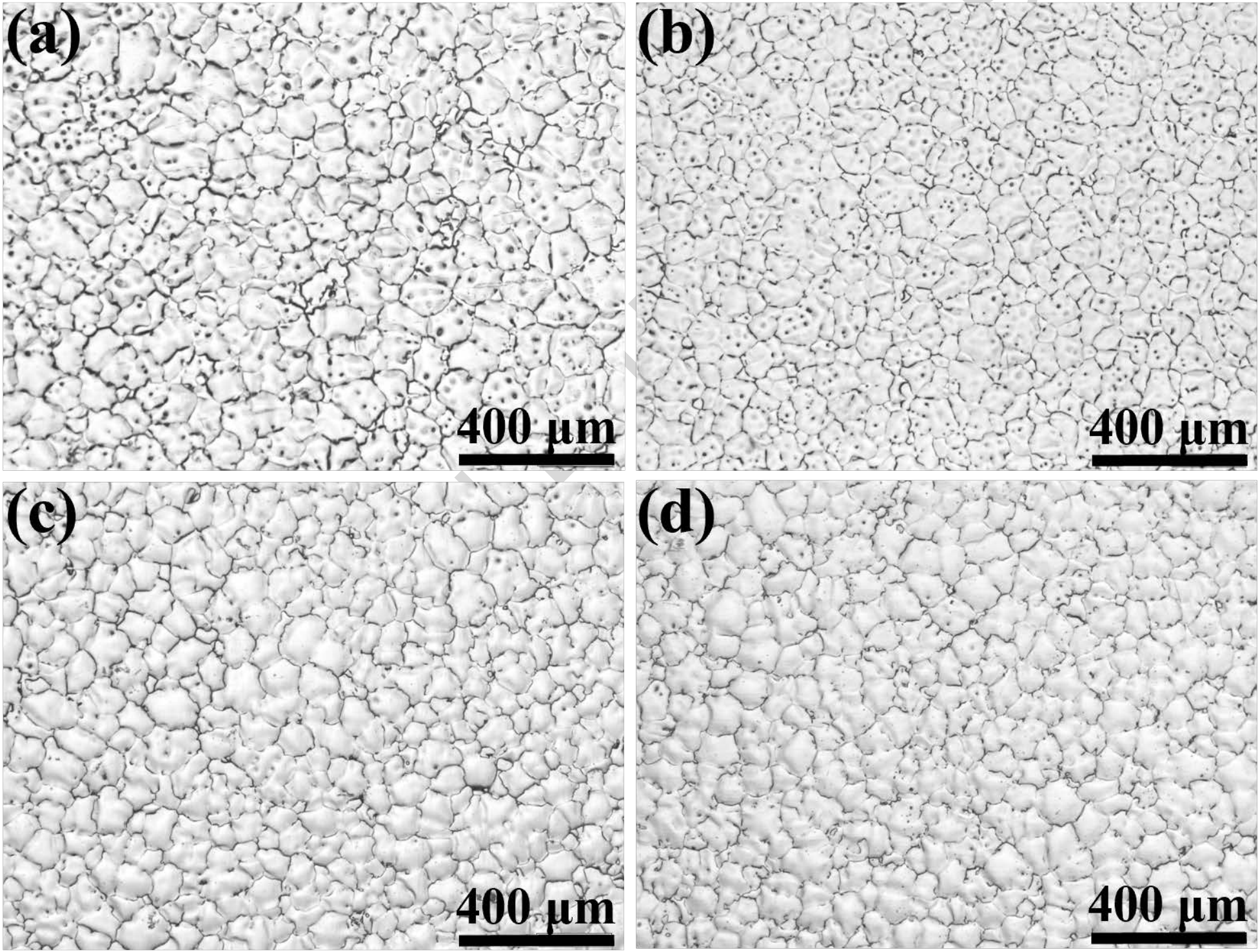

ARTICLE IN PRESS

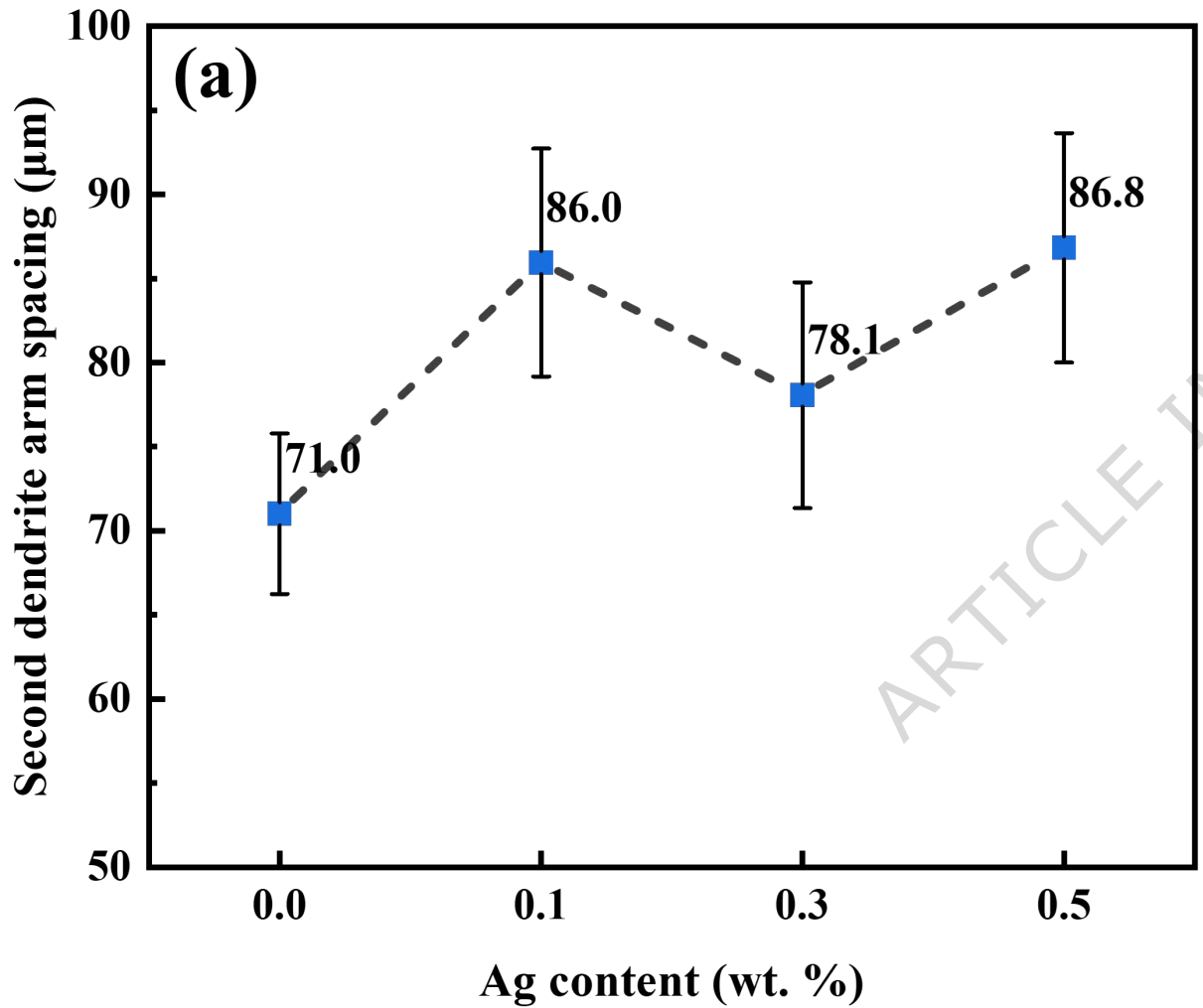

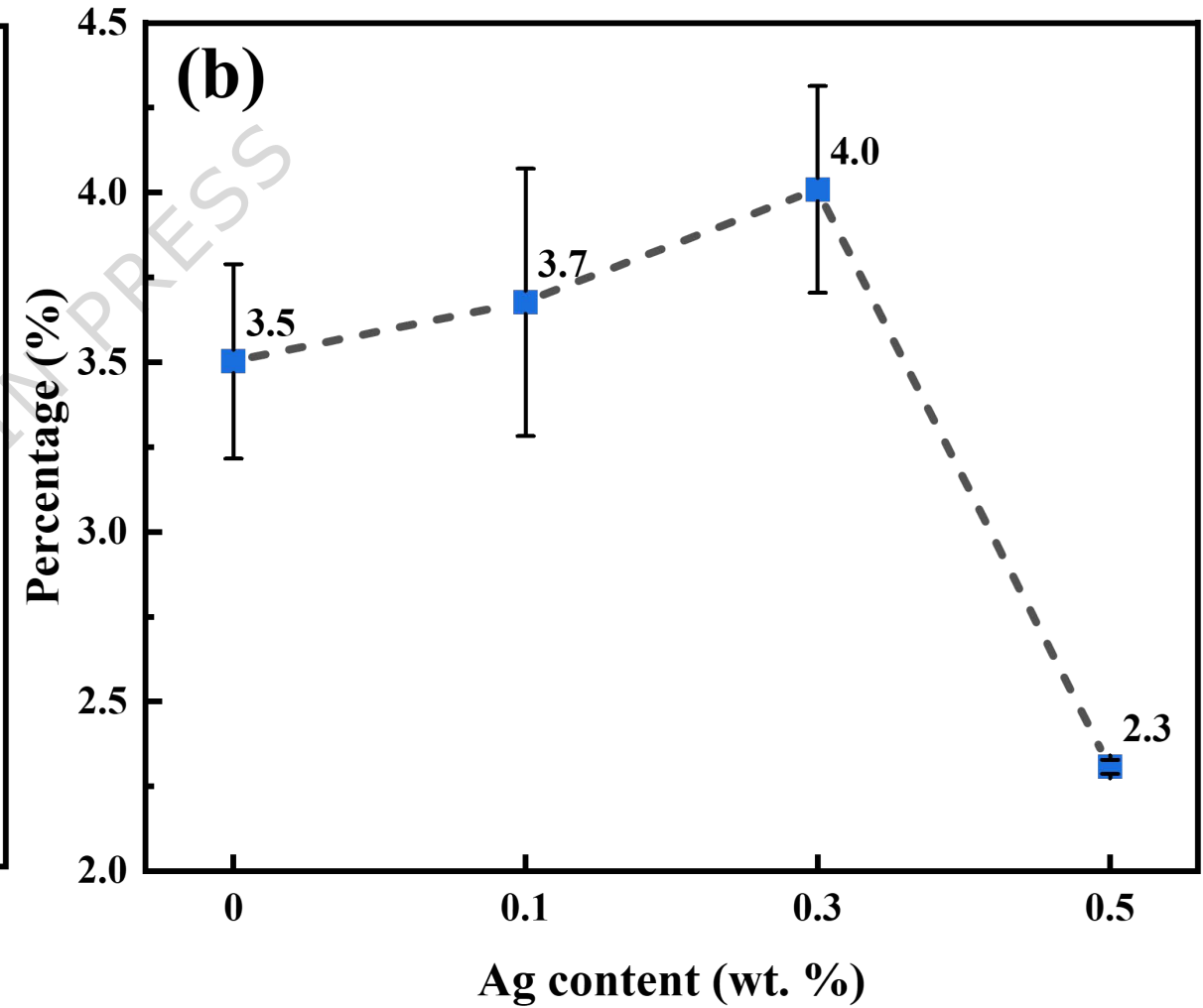

ARTICLE IN PRESS

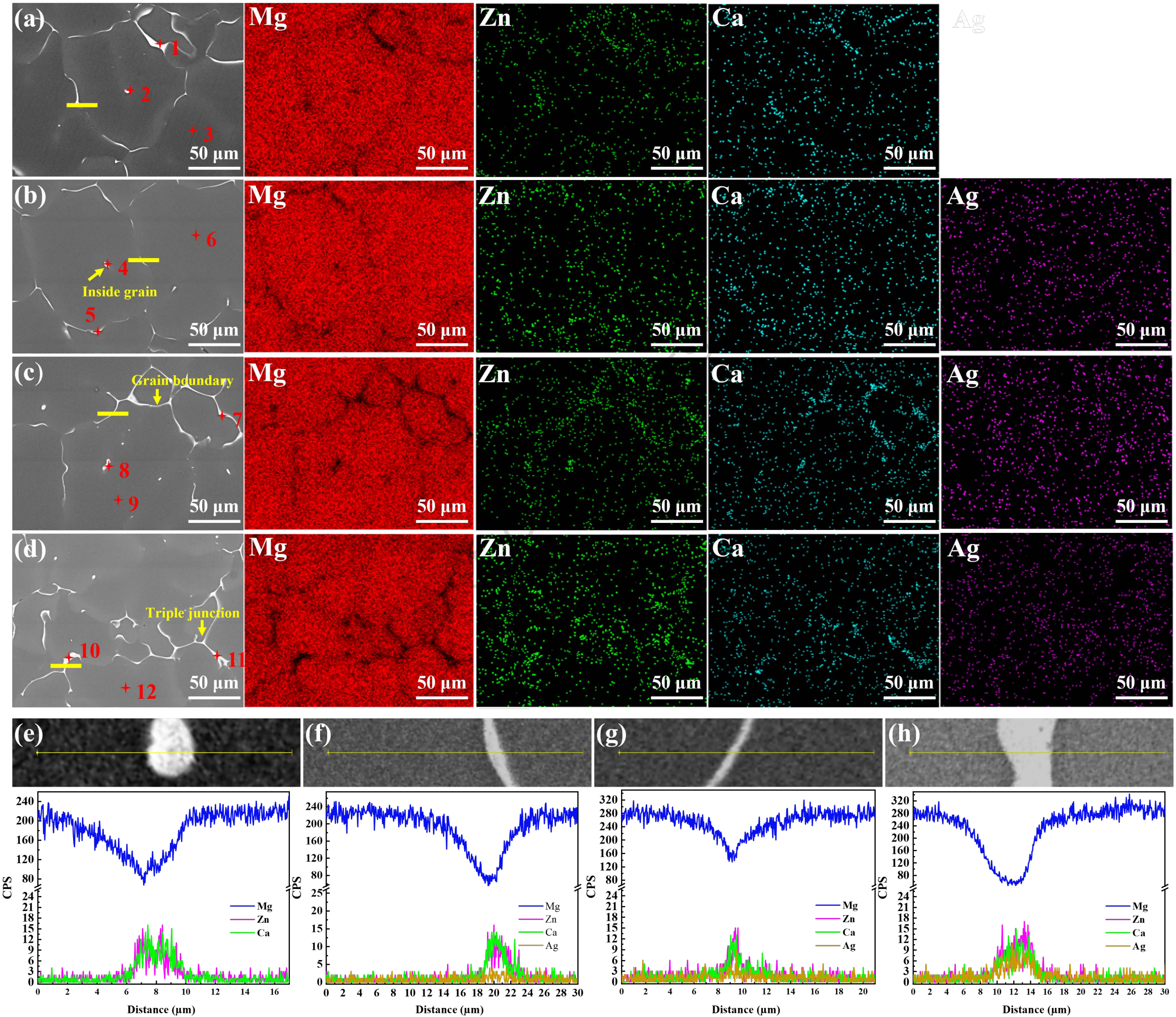
(a)
1
2
3
50 μm
Mg
50 μm
Zn
50 μm
Ca
50 μm
Ag
(b)
6
4
Inside grain
5
50 μm
Mg
50 μm
Zn
50 μm
Ca
50 μm
Ag
50 μm
(c)
Grain boundary
7
8
9
50 μm
Mg
50 μm
Zn
50 μm
Ca
50 μm
Ag
50 μm
(d)
Triple junction
10
11
12
50 μm
Mg
50 μm
Zn
50 μm
Ca
50 μm
Ag
50 μm
(e)
(f)
(g)
(h)
CPS
Distance (μm)
Mg
Zn
Ca
Ag

ARTICLE IN PRESS

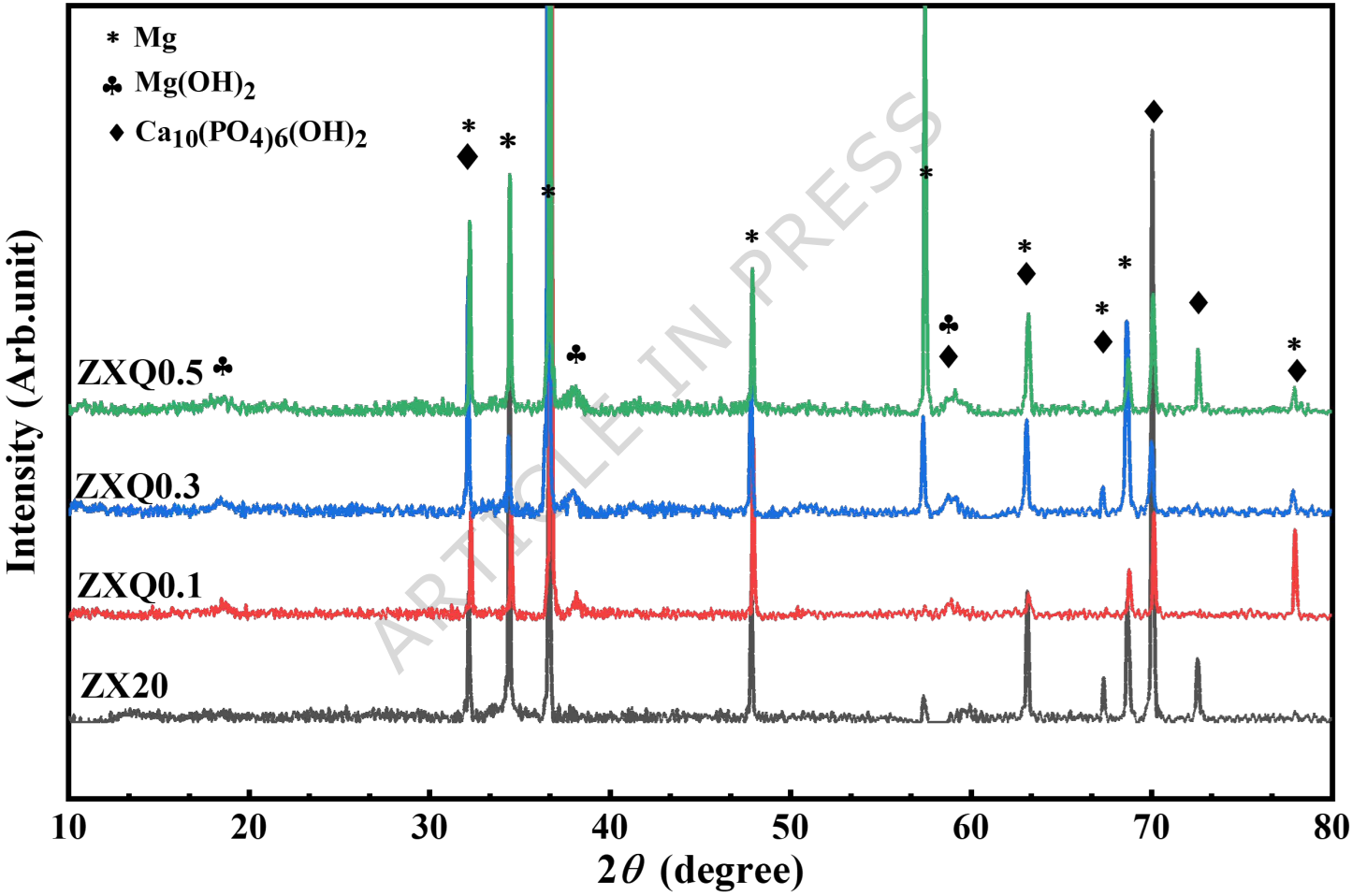

ARTICLE IN PRESS

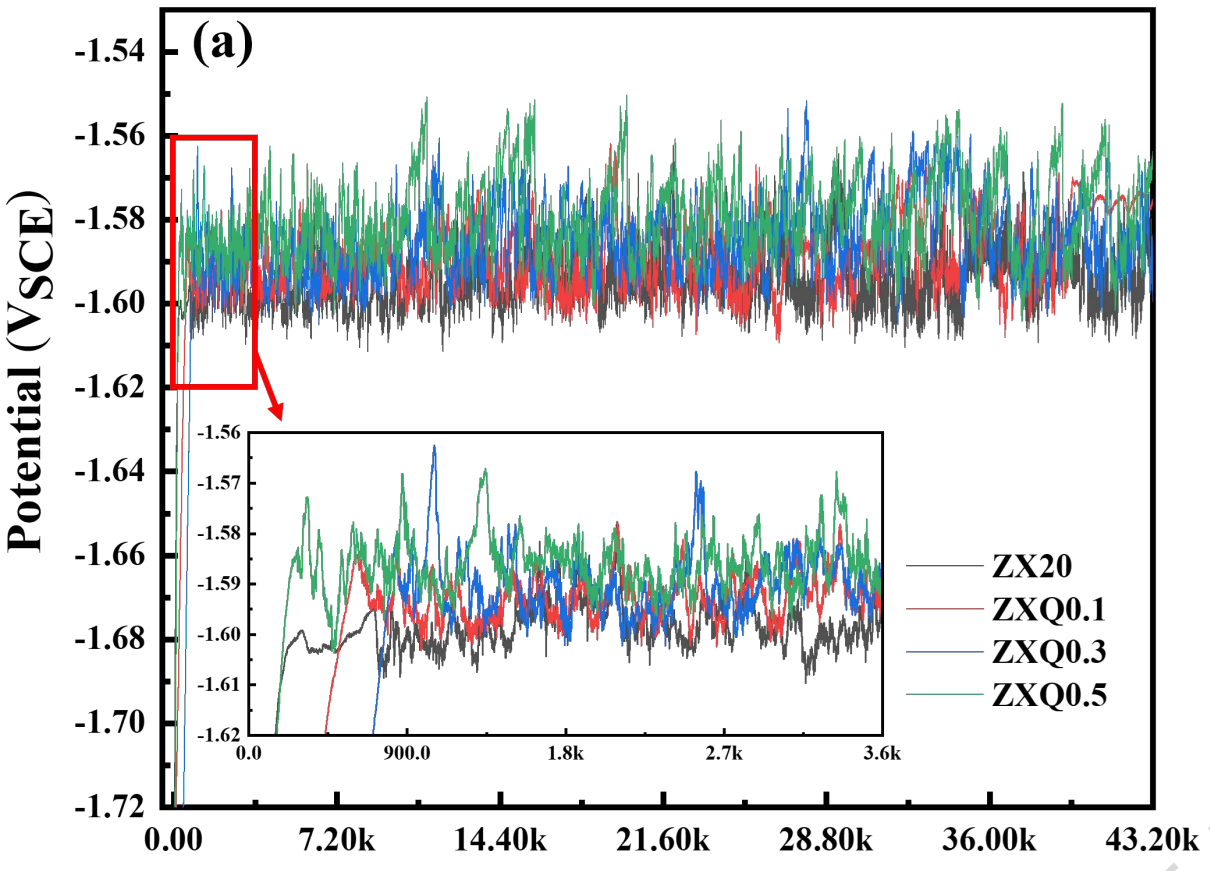
(a)
Potential (V_{SCE})
Time (s)
ZX20
ZXQ0.1
ZXQ0.3
ZXQ0.5

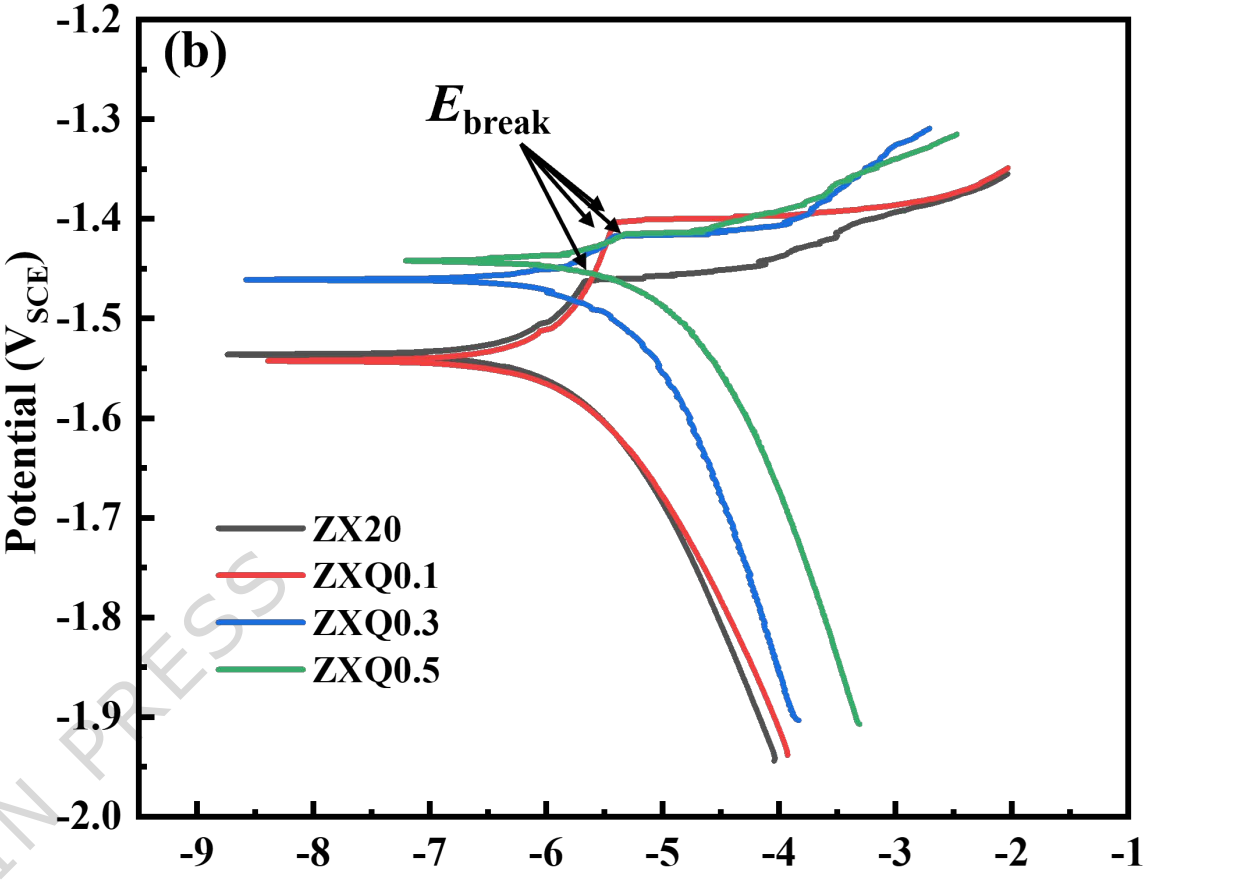
(b)
E_{break}
Potential (V_{SCE})
ZX20
ZXQ0.1
ZXQ0.3
ZXQ0.5

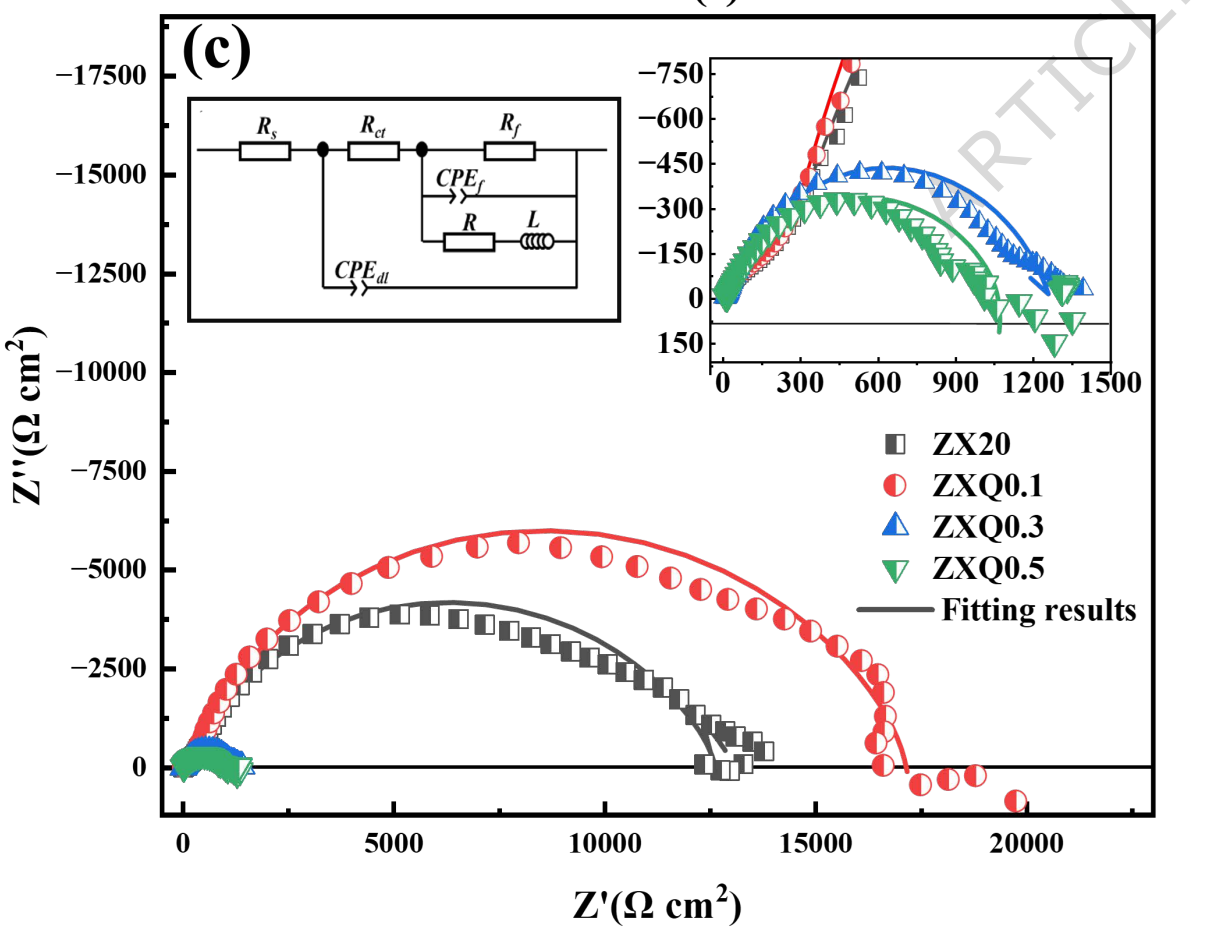
(c)
R_s
R_{ct}
R_f
CPE_f
R
L
CPE_{dl}
Z''(Ω cm^2)
Z'(Ω cm^2)
ZX20
ZXQ0.1
ZXQ0.3
ZXQ0.5
Fitting results

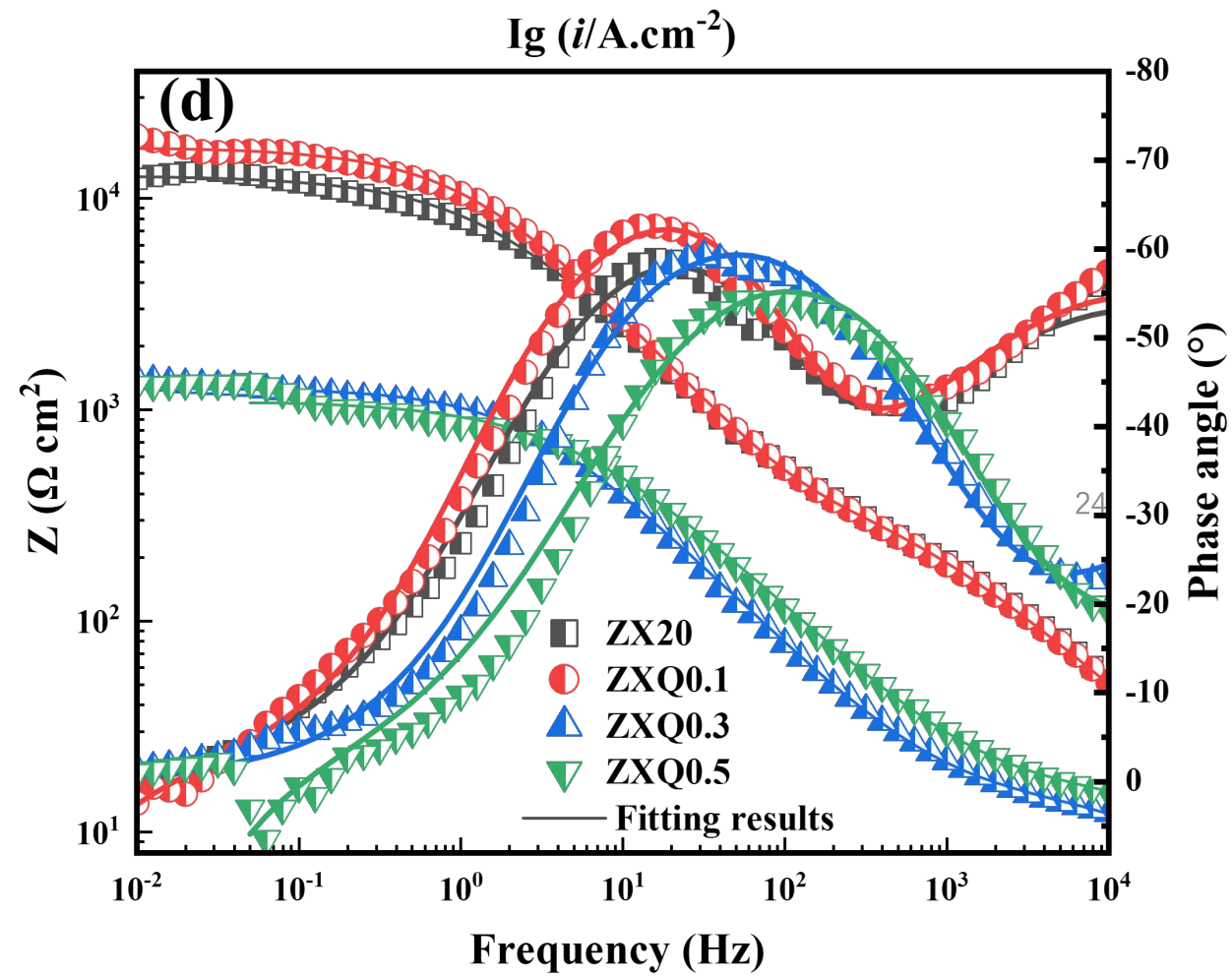
(d)
Ig (i/A.cm^{-2})
Z (Ω cm^2)
Phase angle (°)
Frequency (Hz)
ZX20
ZXQ0.1
ZXQ0.3
ZXQ0.5
Fitting results

ARTICLE IN PRESS

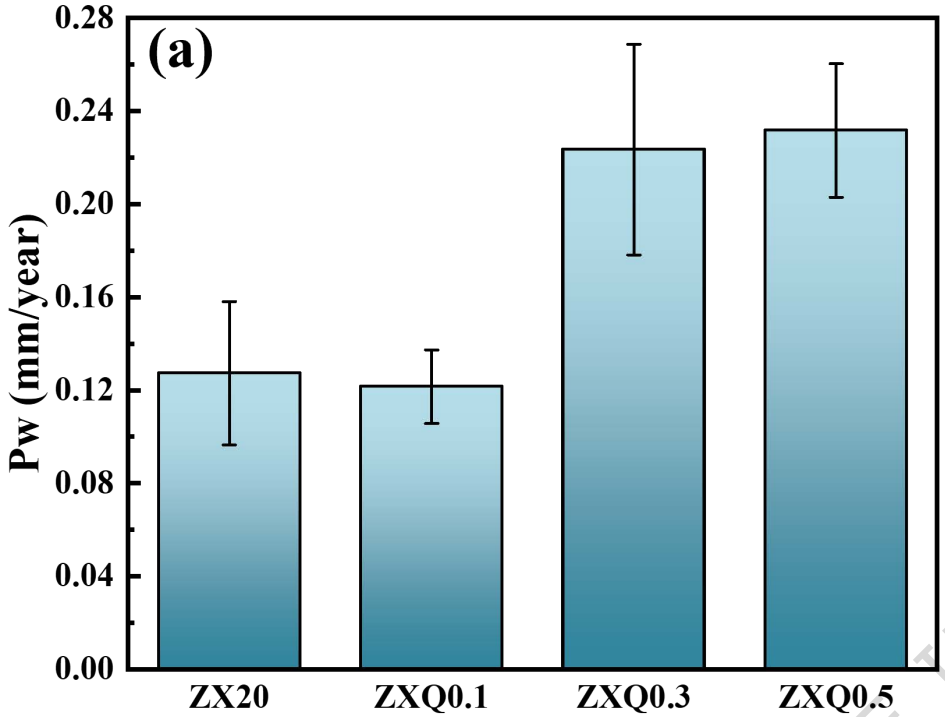

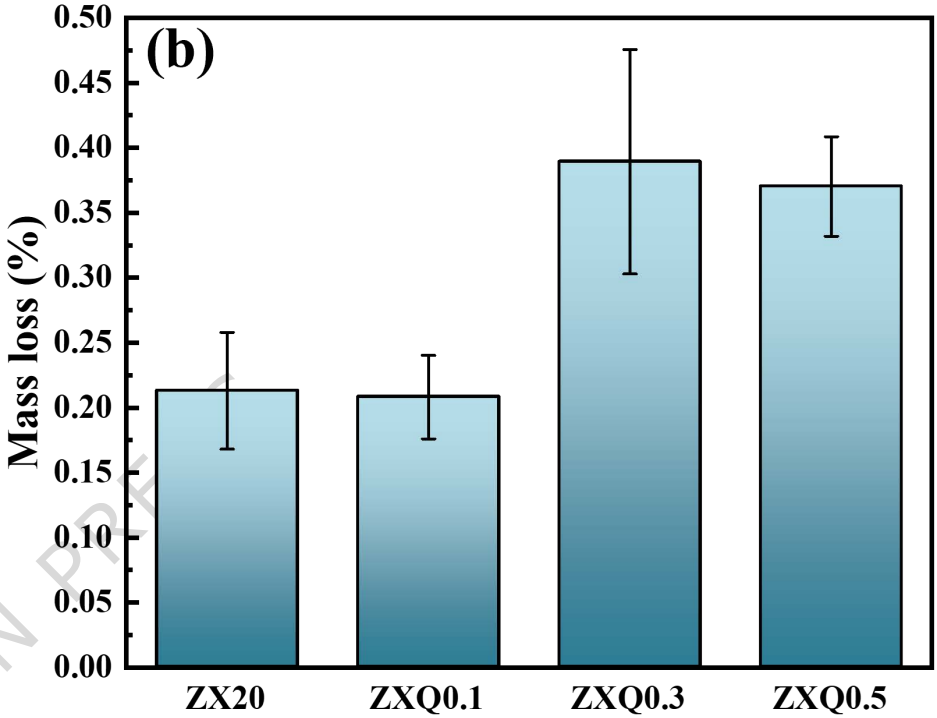

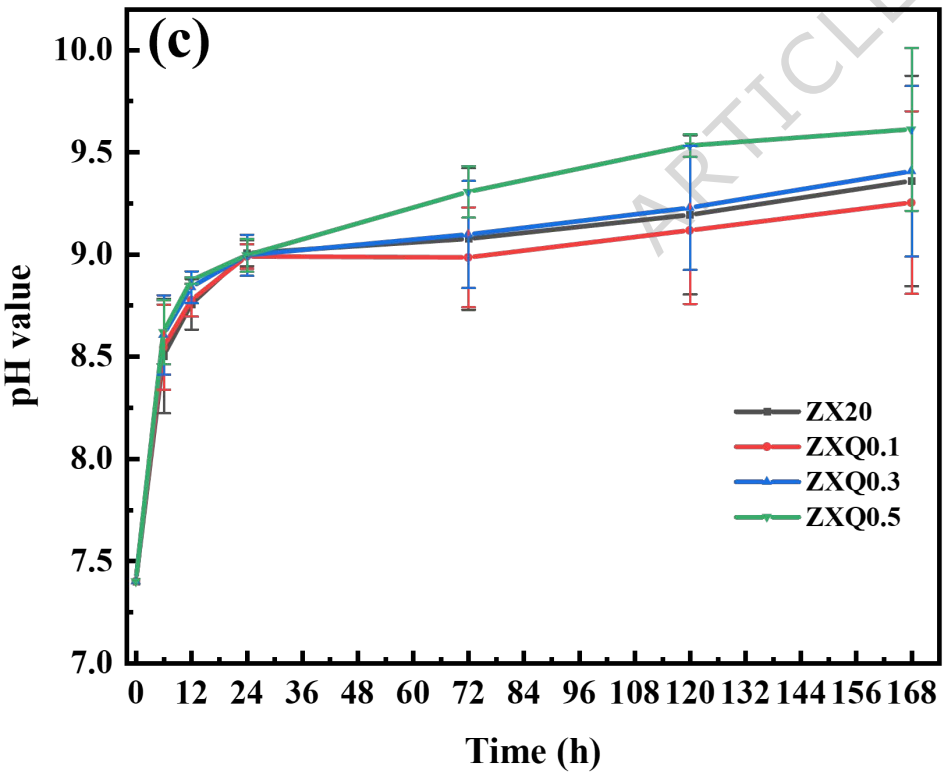

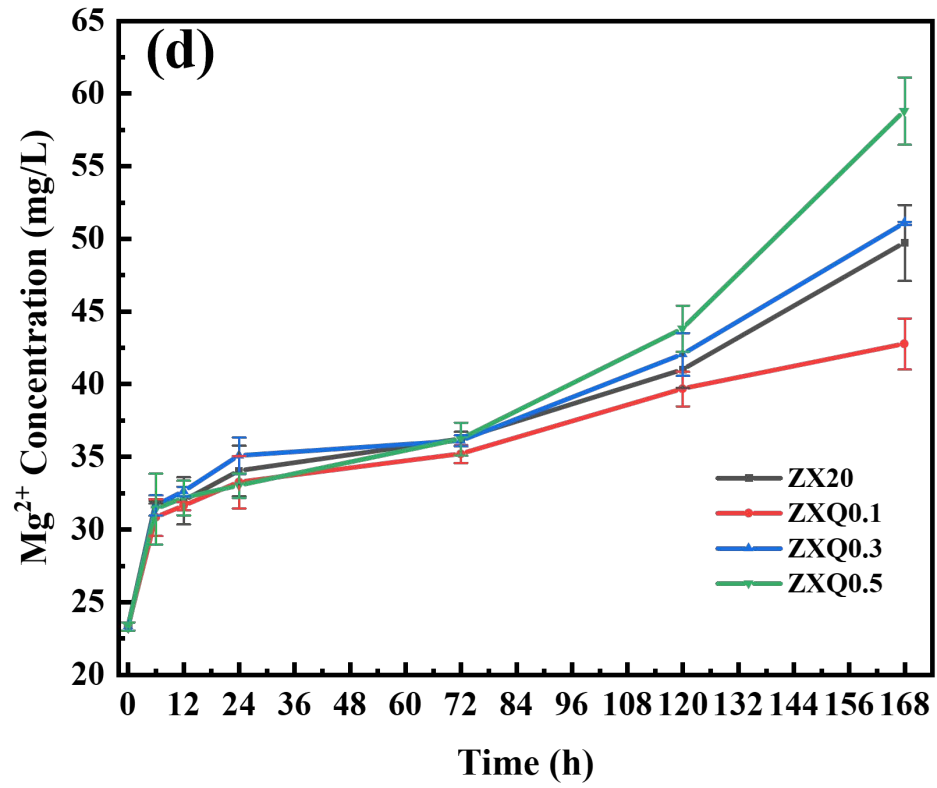

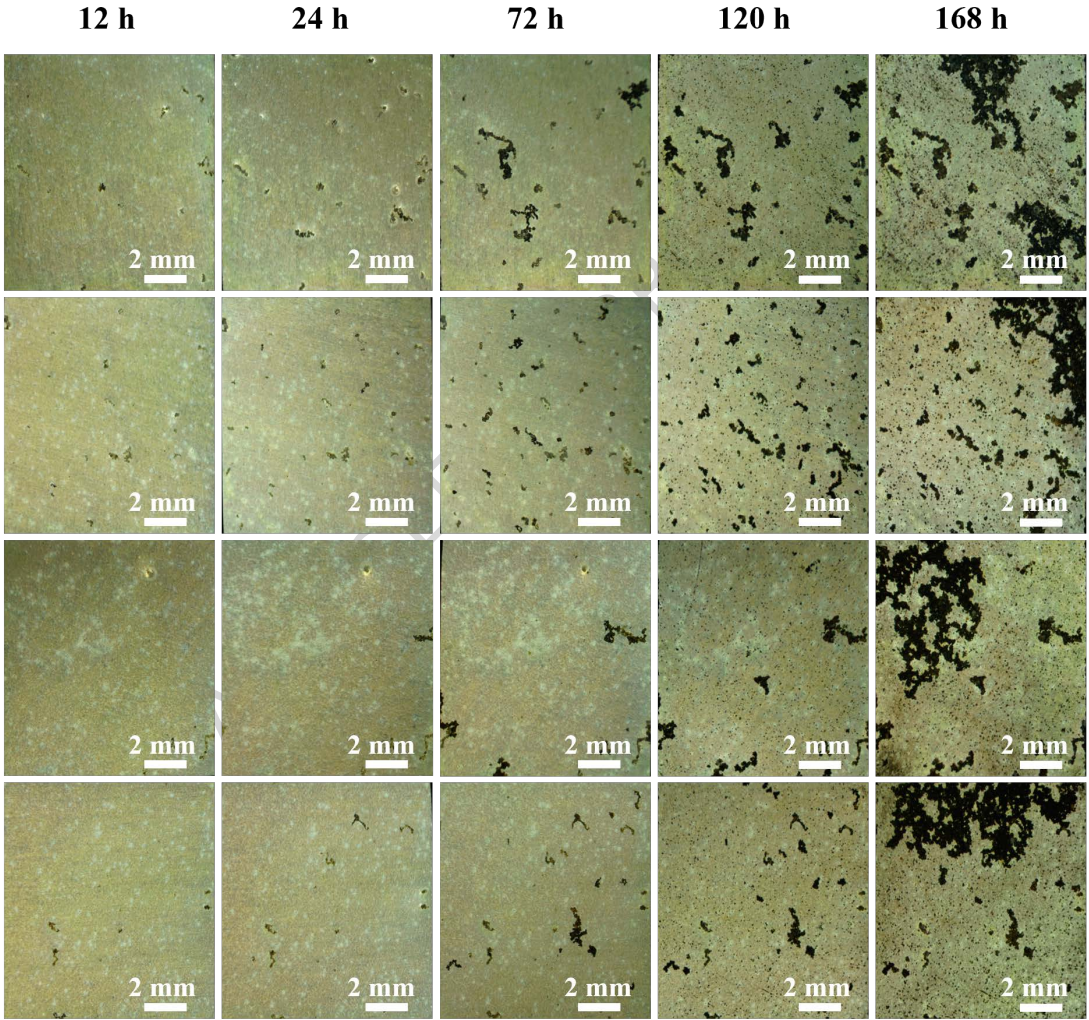
12 h
24 h
72 h
120 h
168 h
ZX20
ZXQ0.1
ZXQ0.3
ZXQ0.5
2 mm

ARTICLE IN PRESS

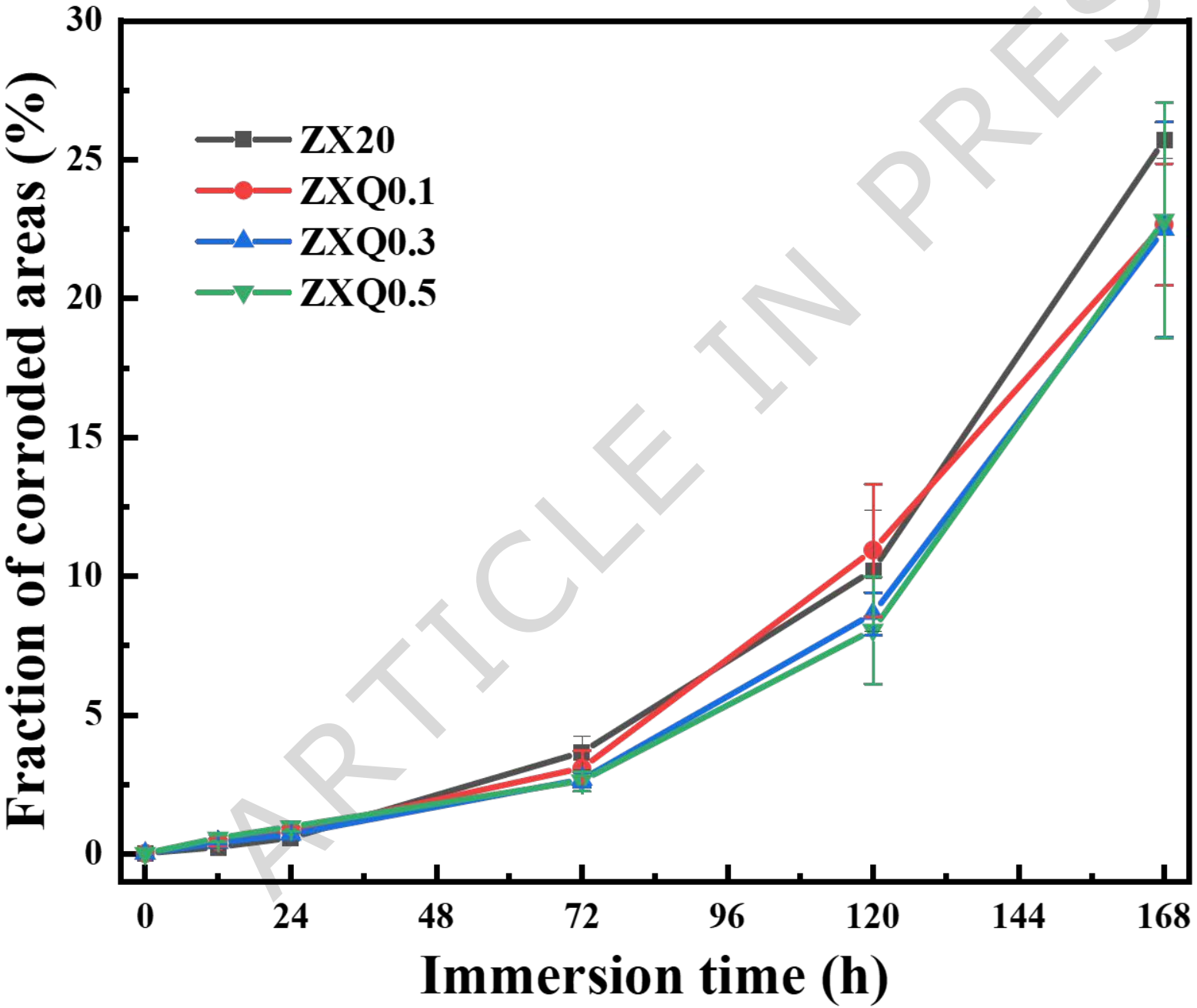

ARTICLE IN PRESS

ARTICLE IN PRESS

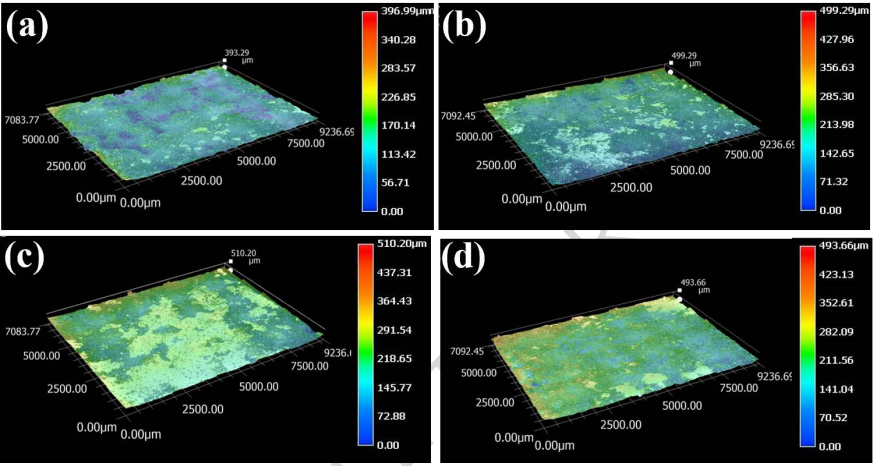

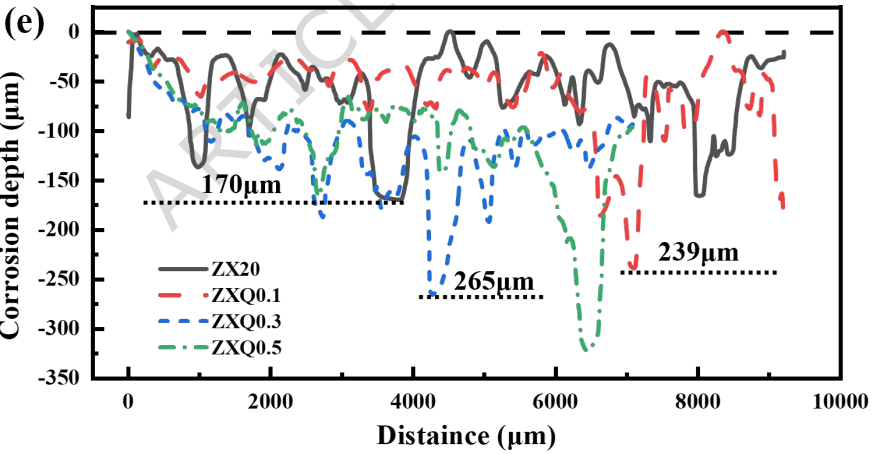

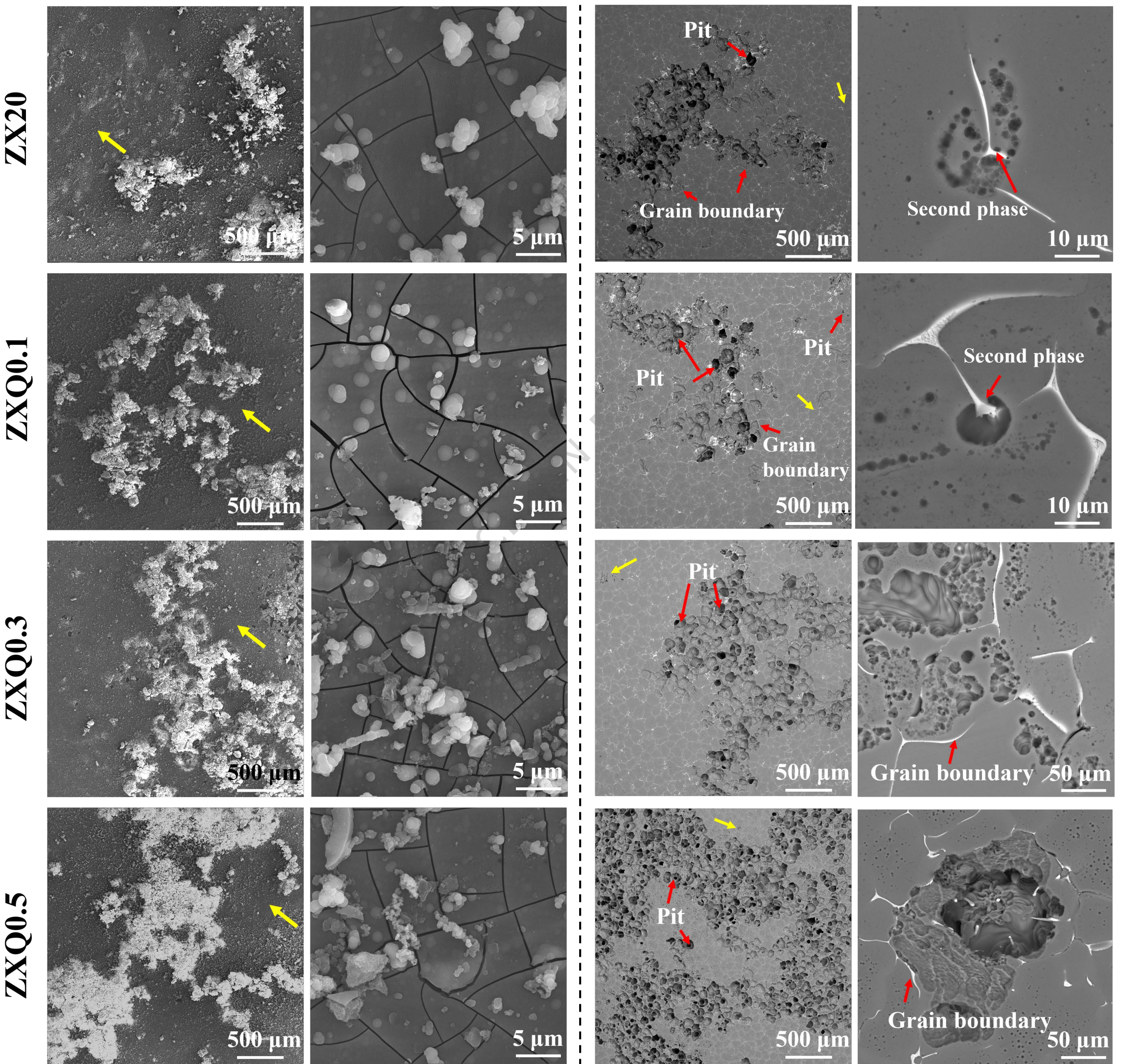
With product
Without product
ZX20
ZXQ0.1
ZXQ0.3
ZXQ0.5
500 μm
5 μm
Pit
Grain boundary
Second phase
10 μm
50 μm

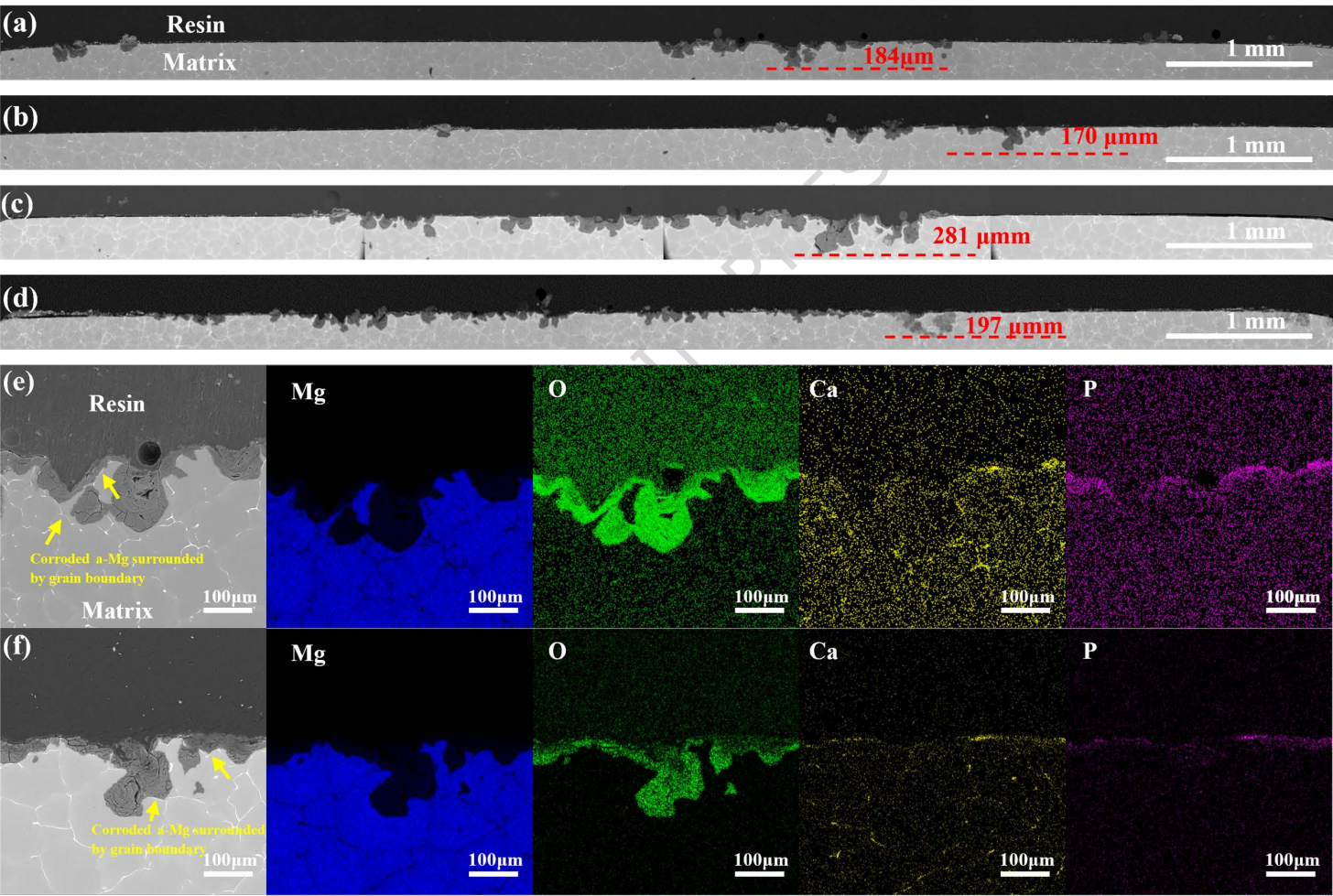
(a)
Resin
Matrix
184μm
1 mm
(b)
170 μmm
1 mm
(c)
281 μmm
1 mm
(d)
197 μmm
1 mm
(e)
Resin
Corroded a-Mg surrounded by grain boundary
Matrix
100μm
Mg
O
Ca
P
(f)
Corroded a-Mg surrounded by grain boundary

ARTICLE IN PRESS

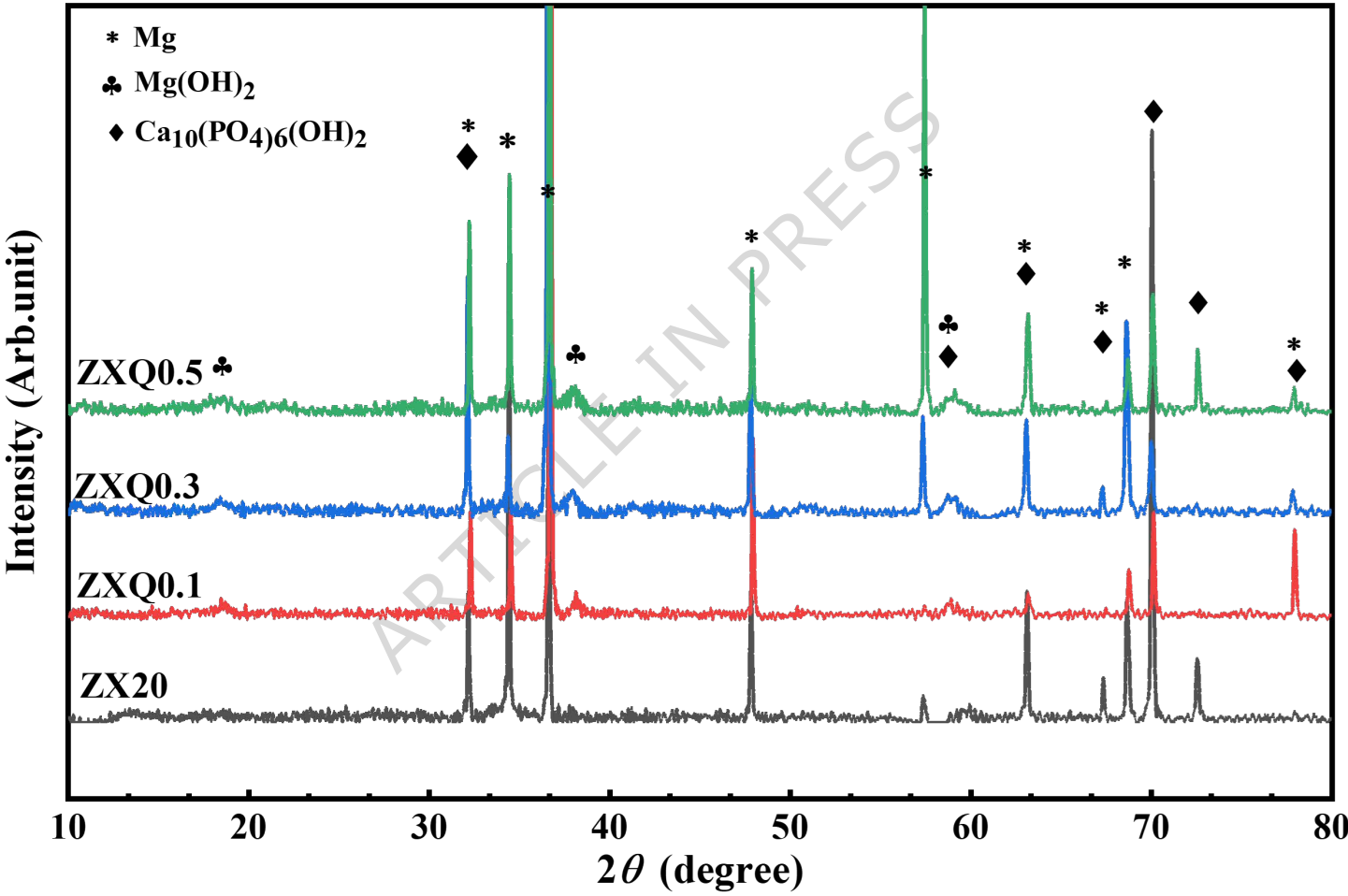

ARTICLE IN PRESS

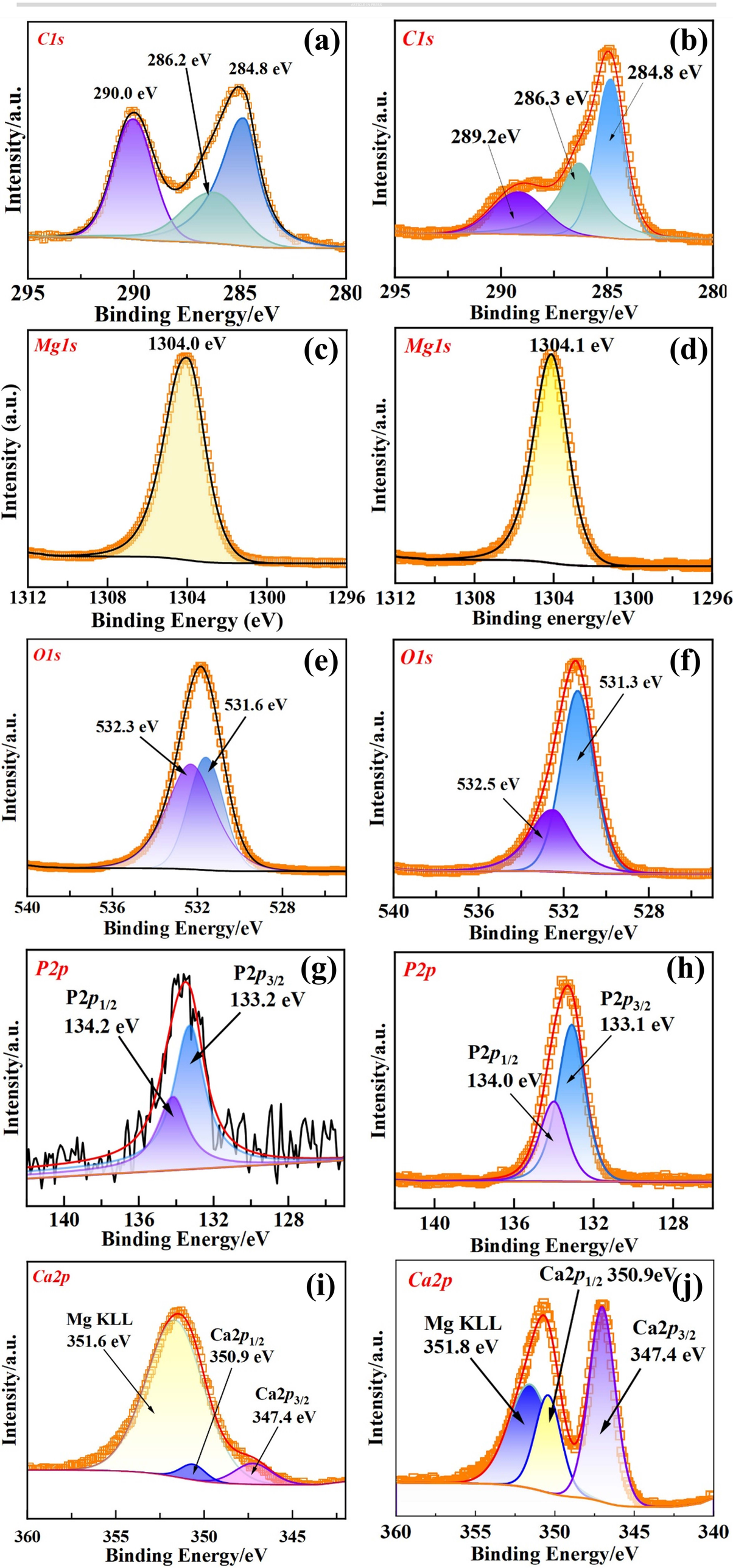
C1s
(a)
286.2 eV
284.8 eV
290.0 eV
Intensity/a.u.
295
290
285
280
Binding Energy/eV
C1s
(b)
284.8 eV
286.3 eV
289.2eV
Intensity/a.u.
295
290
285
280
Binding Energy/eV
Mg1s
1304.0 eV
(c)
Intensity (a.u.)
1312
1308
1304
1300
1296
Binding Energy (eV)
Mg1s
1304.1 eV
(d)
Intensity/a.u.
1312
1308
1304
1300
1296
Binding energy/eV
O1s
(e)
531.6 eV
532.3 eV
Intensity/a.u.
540
536
532
528
Binding Energy/eV
O1s
(f)
531.3 eV
532.5 eV
Intensity/a.u.
540
536
532
528
Binding Energy/eV
P2p
(g)
P2p1/2
134.2 eV
P2p3/2
133.2 eV
Intensity/a.u.
140
136
132
128
Binding Energy/eV
P2p
(h)
P2p3/2
133.1 eV
P2p1/2
134.0 eV
Intensity/a.u.
140
136
132
128
Binding Energy/eV
Ca2p
(i)
Mg KLL
351.6 eV
Ca2p1/2
350.9 eV
Ca2p3/2
347.4 eV
Intensity/a.u.
360
355
350
345
Binding Energy/eV
Ca2p
Ca2p1/2 350.9eV
(j)
Mg KLL
351.8 eV
Ca2p3/2
347.4 eV
Intensity/a.u.
360
355
350
345
340
Binding Energy/eV

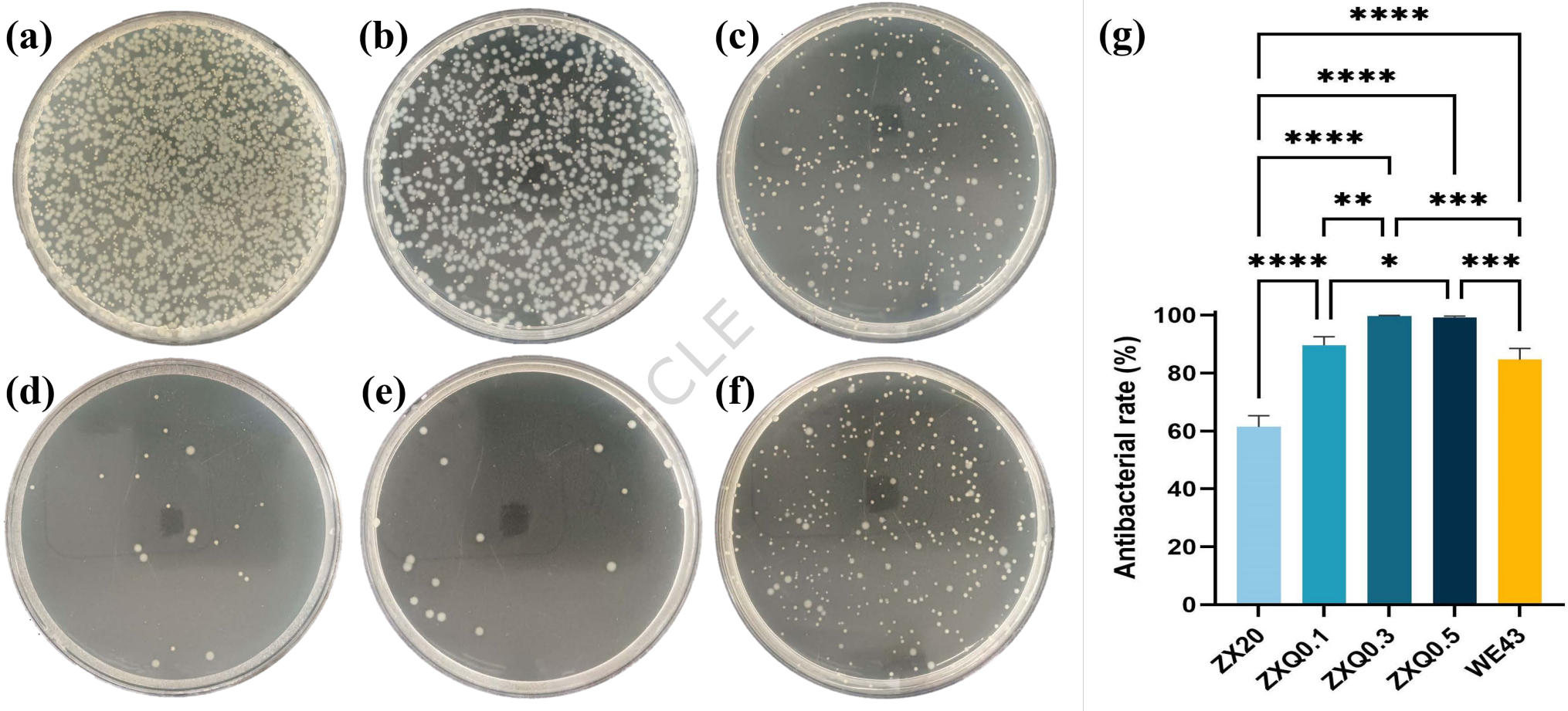
(a)
(b)
(c)
(d)
(e)
(f)
(g)
****
****
****
**
***
****
*
***
Antibacterial rate (%)
100
80
60
40
20
0
ZX20
ZXQ0.1
ZXQ0.3
ZXQ0.5
WE43

ARTICLE IN PRESS